Optics-Free Bioluminescence Detection on a CMOS Camera Chip

by Anna Christoforidou

LUND UNIVERSITY

Division of Solid State Physics and NanoLund

Thesis for the degree of
Master of Science in Nanoscience

Supervisor: Heiner Linke
Co-supervisor: Nils Gustafsson

Examiner: Carina Fasth

May 29, 2026

ABSTRACT

This thesis explores the development of a compact, optics free and low-cost biosensing platform based on direct on-chip detection of bioluminescence using a complementary metal–oxide–semiconductor (CMOS) image sensor. This work is motivated by the need and challenge of combining the high sensitivity of optical biosensing in laboratories with the simplicity and portability required for point-of-care applications. More specifically, we calibrated a commercial CMOS camera sensor and evaluated it as a quantitative detector for low-light measurements by characterizing its responsivity, linearity, noise floor, and saturation behavior under controlled LED illumination. In parallel, we expressed, purified and characterized a bioluminescent reporter system based on NanoLuc luciferase using UV–Vis spectroscopy and SDS–PAGE analysis. Lastly, we integrated these two elements into a biosensing device using accessible methods, including 3D-printed components and a PDMS sample well positioned directly above the sensor surface area. Baseline experiments demonstrated successful direct detection of NanoLuc bioluminescence down to 10nM, using the CMOS platform, while a microscopy-based setup served as a reference system for comparison. To improve detection sensitivity under weak-signal conditions below 10 nM, we proposed and demonstrated a signal enhancement approach based on lock-in amplification using a microfluidic modulation platform in a microscope-based setup. These findings highlight the potential of modulation-based signal processing for future highly sensitive and portable optical biosensing applications.

POPULAR SUMMARY

During the COVID-19 pandemic, rapid antigen tests introduced many people to biosensors, although (knowingly or not) people had already been using biosensors such as pregnancy tests or smartwatches that monitor heartbeat for years. In fact, any system that combines a biological recognition element with a transducer that converts detection into a readable signal is, by definition, a biosensor.

To explain this with the COVID-19 test example, in this case the biological recognition element is an antibody tagged with a gold nanoparticle, that specifically binds to molecules from the virus (important note: please do not open a COVID-19 test trying to retrieve the gold nanoparticles). When enough of these virus - antibody - gold systems accumulate on the test strip, they form the visible red line indicating a positive result. Interestingly, gold nanoparticles are not actually gold-colored at all, but can appear red, blue, or green depending on their size and arrangement (the bright colors in stained-glass church windows are a centuries-old example of this effect). Back to the transducer element, which, in this case, is simply the human eye, that detects and interprets the red line.

The human eye is remarkably sensitive in low-light conditions (and probably the cheapest detector you can find — it comes for free!). It can usually tell us whether something is present or not, and sometimes even whether there is “a little” or “a lot” of it. However, the eye is not truly a quantitative detector. In many medical situations, doctors care not only about whether a biomarker exists, but also about its concentration and how it changes over time, since small changes can reveal whether a disease is progressing or whether a treatment is working.

Today, highly sensitive quantitative biological measurements are already possible using advanced laboratory techniques such as Polymerase Chain Reaction (PCR) and fluorescence microscopy. The problem is that these methods often require expensive equipment, specialized laboratories, and trained personnel. Because of this, they are usually only used once symptoms become serious enough to justify complex testing. This is not ideal for diseases such as cancer or sepsis, which may begin with extremely small biological changes and vague symptoms that initially look no different from a common cold or simple fatigue. Of course, it would be impossible, both practically and economically, to send every patient with generic symptoms for highly specialized laboratory analysis. This creates a gap between highly sensitive laboratory diagnostics and simple point-of-care tests that can be used quickly and routinely in everyday healthcare.

This thesis explores a possible middle ground by combining bioluminescence with a CMOS camera, similar to the ones found in smartphones, to create a simple optical biosensing platform. In this system, bioluminescence acts as the biological signal generation mechanism, while the CMOS camera, adapted for low-light detection, converts light signals into measurable digital information.

Bioluminescence produces light directly through a chemical reaction, similar to how fireflies glow in nature. Since the light is generated internally, there is no need for external light sources such as lasers or complicated optical components and alignment, making the system potentially simpler, cheaper and more portable, than most techniques used in laboratories nowadays. To investigate this idea, we expressed a highly bright bioluminescent protein called NanoLuc and integrated it into a custom-built sensing platform positioned directly above the CMOS camera (see super cool Fig. IV.2a). The results of this thesis showed that relatively weak bioluminescent signals could be detected directly on the sensor. In addition, a proof-of-concept signal enhancement approach, called lock-in amplification, was explored to investigate whether sensitivity could be further improved under extremely low-light conditions.

In the long term, systems like this could contribute to portable biosensors capable of detecting diseases earlier and more routinely outside specialized laboratories. Beyond medical diagnostics, similar technologies could also find applications in areas such as food safety and environmental monitoring. Imagine a future where biosensors like these become as integrated into everyday life as pregnancy tests are today. Making reliable scientific measurements more accessible in everyday life could not only improve quality of life, but also help strengthen public trust and interest in science at a time when misinformation and pseudoscience are increasingly widespread.

ΔΗΜΟΦΙΛΗΣ ΠΕΡΙΛΗΨΗ

Κατά τη διάρκεια της πανδημίας COVID-19, τα rapid antigen tests σύστησαν σε πολύ κόσμο τους βιοαισθητήρες, αν και στην πραγματικότητα οι άνθρωποι χρησιμοποιούσαν ήδη βιοαισθητήρες (γνωριζοντάς το ή όχι), όπως τα τεστ εγκυμοσύνης και τα smartwatches που παρακολουθούν τον καρδιακό παλμό, εδώ και χρόνια. Στην πραγματικότητα, οποιοδήποτε σύστημα συνδυάζει ένα βιολογικό στοιχείο αναγνώρισης με έναν μετατροπέα που μετατρέπει την βιολογική ανίχνευση σε ένα αναγνώσιμο σήμα είναι, εξ ορισμού, ένας βιοαισθητήρας.

Για να εξηγίσουμε αυτόν τον ορισμό με ένα οικείο παράδειγμα, σε ένα τεστ COVID-19 το βιολογικό στοιχείο αναγνώρισης είναι ένα αντίσωμα του ιού συνδεδεμένο με νανοσωματίδια χρυσού. Το αντίσωμα δένεται εξόρισμού σε μόρια του ιού (σημαντική σημείωση: μην ανοίξετε ένα τεστ COVID-19 προσπαθώντας να πάρετε τα νανοσωματίδια χρυσού). Όταν αρκετά από αυτά τα συστήματα ιού – αντισώματος – νανοσωματιδίου χρυσού συσσωρευτούν πάνω στη δοκιμαστική ταινία, σχηματίζουν τη χαρακτηριστική κόκκινη γραμμή που υποδεικνύει θετικό αποτέλεσμα. Είναι ενδιαφέρον ότι τα νανοσωματίδια χρυσού δεν έχουν στην πραγματικότητα χρυσαφί χρώμα, αλλά μπορούν να εμφανίζονται κόκκινα, μπλε ή πράσινα, ανάλογα με το μέγεθος και τη διάταξή τους (τα έντονα κόκκινα χρώματα στα βιτρό των εκκλησιών αποτελούν ένα χαρακτηριστικό παράδειγμα αυτού του φαινομένου). Όσον αφορά το στοιχείο του μετατροπέα, σε αυτή την περίπτωση είναι απλώς το ανθρώπινο μάτι, το οποίο ανιχνεύει και ερμηνεύει την κόκκινη γραμμή.

Το ανθρώπινο μάτι είναι εντυπωσιακά ευαίσθητο σε συνθήκες χαμηλού φωτισμού (και πιθανότατα ο φθηνότερος ανιχνευτής που μπορεί να βρει κανείς — έρχεται δωρεάν!). Μπορεί να μας πει αν κάτι υπάρχει ή όχι, και μερικές φορές ακόμη και αν υπάρχει ‘λίγο’ ή ‘πολύ’. Ωστόσο, το μάτι δεν είναι πραγματικά ένας ποσοτικός ανιχνευτής. Σε πολλές ιατρικές περιπτώσεις, οι γιατροί δεν ενδιαφέρονται μόνο για το αν υπάρχει ένας βιοδείκτης, αλλά και για τη συγκέντρωσή του και το πώς αυτή αλλάζει με τον χρόνο, καθώς μικρές μεταβολές μπορούν να αποκαλύψουν αν μια ασθένεια εξελίσσεται ή αν μια θεραπεία λειτουργεί.

Σήμερα, εξαιρετικά ευαίσθητες ποσοτικές βιολογικές μετρήσεις είναι ήδη δυνατές μέσω προηγμένων εργαστηριακών τεχνικών, όπως το PCR και η μικροσκοπία φθορισμού. Το πρόβλημα είναι ότι αυτές οι μέθοδοι συχνά απαιτούν ακριβό εξοπλισμό, εξειδικευμένα εργαστήρια και εκπαιδευμένο προσωπικό. Εξαιτίας αυτού, συνήθως χρησιμοποιούνται μόνο όταν τα συμπτώματα γίνουν αρκετά σοβαρά ώστε να δικαιολογούν τόσο πολύπλοκες εξετάσεις. Αυτό δεν είναι ιδανικό για ασθένειες όπως ο καρκίνος ή η σήψη, οι οποίες μπορεί να ξεκινούν με εξαιρετικά μικρές βιολογικές αλλαγές και ασαφή συμπτώματα που αρχικά δεν διαφέρουν από ένα κοινό κρυολόγημα ή απλή κόπωση. Φυσικά, θα ήταν αδύνατο, τόσο πρακτικά όσο και οικονομικά, να αποστέλλεται κάθε ασθενής με γενικά συμπτώματα για εξειδικευμένες εργαστηριακές αναλύσεις. Έτσι δημιουργείται ένα κενό ανάμεσα στις εξαιρετικά ευαίσθητες εργαστηριακές διαγνώσεις και στα απλά point-of-care τεστ που μπορούν να χρησιμοποιηθούν γρήγορα και συστηματικά στην καθημερινότητα.

Αυτή η εργασία εξερευνά μια πιθανή ενδιάμεση λύση, συνδυάζοντας τη βιοφωταύγεια με μια κάμερα CMOS, παρόμοια με αυτές που βρίσκονται στα smartphones, ώστε να δημιουργηθεί ένας απλός οπτικός βιοαισθητήρας. Σε αυτό το σύστημα, η βιοφωταύγεια λειτουργεί ως ο μηχανισμός παραγωγής του βιολογικού σήματος, ενώ η κάμερα, προσαρμοσμένη για ανίχνευση χαμηλού φωτισμού, μετατρέπει τα φωτεινά σήματα σε μετρήσιμες ψηφιακές πληροφορίες.

Η βιοφωταύγεια παράγει φως απευθείας μέσω μιας χημικής αντίδρασης, παρόμοια με τον τρόπο που λάμπουν οι πυγολαμπίδες στη φύση. Εφόσον το φως παράγεται εσωτερικά, δεν απαιτούνται εξωτερικές πηγές φωτός, όπως λέιζερ ή πολύπλοκα οπτικά εξαρτήματα και ευθυγραμμίσεις, γεγονός που καθιστά το σύστημα δυνητικά απλούστερο, φθηνότερο και πιο φορητό σε σύγκριση με τις περισσότερες τεχνικές που χρησιμοποιούνται σήμερα στα εργαστήρια. Για τον σκοπό αυτό, παράξαμε μια εξαιρετικά φωτεινή βιοφωταυγή πρωτεΐνη, την NanoLuc, και την ενσωματώσαμε σε μια ειδικά κατασκευασμένη πλατφόρμα ανίχνευσης τοποθετημένη ακριβώς πάνω από την κάμερα (βλέπε IV .2α). Τα αποτελέσματα αυτής της εργασίας έδειξαν ότι σχετικά ασθενή βιοφωταυγή σήματα μπορούσαν να ανιχνευθούν απευθείας πάνω στον αισθητήρα. Επιπλέον, αποδείξαμε οτι η τεχνική ενίσχυσης σήματος, γνωστή ως λοςκ-ιν αμπλιφιςατιον, είναι συμβατή με τον αισθητήρα μας, βελτιώνοντας περαιτέρω την εθαισθησία του υπό συνθήκες εξαιρετικά χαμηλού φωτισμού..

Μακροπρόθεσμα, συστήματα όπως αυτό θα μπορούσαν να συμβάλουν στην ανάπτυξη φορητών βιοαισθητήρων ικανών να ανιχνεύουν ασθένειες νωρίτερα και πιο συστηματικά εκτός εξειδικευμένων εργαστηρίων. Πέρα από τις ιατρικές διαγνώσεις, παρόμοιες τεχνολογίες θα μπορούσαν επίσης να βρουν εφαρμογές σε τομείς όπως ο ποιοτικός έλεγχος τροφίμων και η περιβαλλοντική παρακολούθηση. Φανταστείτε ένα μέλλον όπου βιοαισθητήρες σαν αυτούς θα είναι τόσο ενσωματωμένοι στην καθημερινή ζωή όσο είναι σήμερα τα τεστ εγκυμοσύνης. Η διάθεση αξιόπιστων επιστημονικών μετρήσεων στο ευρύ κοινό θα μπορούσε όχι μόνο να βελτιώσει την ποιότητα ζωής, αλλά και να ενισχύσει την εμπιστοσύνη και το ενδιαφέρον του κοινού προς την επιστήμη, σε μια εποχή όπου η παραπληροφόρηση και η ψευδοεπιστήμη εξαπλώνονται ολοένα και περισσότερο.

ACKNOWLEDGEMENTS

To **Heiner**, thank you for trusting me throughout this project, for giving me the creative freedom to explore ideas, and for creating an inclusive and welcoming group environment.

To **Nils**, thank you for your guidance, organization, and lab expertise throughout this work. Your ability to bring clarity to overwhelming moments, together with your rare but impactful life advice, is very appreciated.

To **Amijai**, for being patient with a physist trying to get into protein expression and characterization, as well as all inspiring conversations we had during our walks in between physics and chemistry.

To **Julia**, thank you for being one of the most welcoming and open people not only in our group but in the FTF in general (and thanks for every morning coffee you made ever).

To **Ruby**, thank you for being both an inspiration and a reminder that science should always include a bit (or more) of fun.

To the **entire Linke group**, it was lovely being part of such an awesome group, thanks.

To **Dan**, you are the best master coordinator, thanks. The Friday FTF fika meetings were always the perfect end to the week with your jokes. I especially appreciate how seriously you always took my endless questions.

To my group mate, but most importantly my office mate and eternal scientific nemesis, **Noah** — thank you for bringing the right amount of chaos and spice into everyday life in the office.

To my uni friends **Laura**, **Sophie**, and **Rafaela**, thank you for sharing this en-

tire master's journey with me. We somehow made it through alive, and I could not have asked for better people to celebrate the highs and survive the lows with.

To all of my roommates, past and present (yes, all 37 of you) thank you for turning **Greenhouse** into a real community and a true home during these two years. From spontaneous dance parties and karaoke sessions to shared dinners during dark winter nights, snow fights, support, and laughter, you made everyday life brighter and unforgettable. A special mention goes to **Smaragda**, **Anna**, and **Andrew**. As Anna always says, "if you want the village you need to be the village" and you truly were the best village anyone could ask for — the OGs.

To my bros, **Matilde** and **Leo**, I wish you had stayed longer. It's hard to describe with words the weird bond we have, but it's there and I'll always cherish it.

To my tennis mates, **Jakob** and **Clémence**, thank you for the stress-releaf tennis sessions and all the fun times afterward. You two are genuinely too cool for me.

To **Emily**, thank you for being such a special person. You constantly inspired me to try new things and somehow always fit into impossibly tight spaces.

To my Greek girls — **Jenny**, **Vaitsa**, **Domna**, **Savvina** and **Elena**, thank you for being the touch of home, comfort, and gossip that I needed while living in Sweden.

To my friends back home — **Eleni**, **Ioanna**, **Sofia**, **Dimitra**, and **Katerina** , thank you for never forgetting about me and for always making me feel as though no time or distance had passed. I will always treasure our years together studying physics.

Last but certainly not least, to my family, **Μαμά**, **Μπαμπά**, **Χάρη**, and all my extended family, thankfully large enough to forgive me for not mentioning everyone by name, thank you for allowing me to pursue my studies free from worry and for always supporting me emotionally and financially with unconditional love and confidence.Σας αγαπώ πολύ.

CONTENTS

I INTRODUCTION

Biosensing, defined as the detection and quantification of biological molecules, plays a central role in scientific research due to its wide range of applications, including environmental monitoring, food safety, and clinical diagnostics, all of which contribute to improving everyday life [1]. In particular, rapid, reliable and sensitive biosensing is central to point-of-care (POC) diagnostics, where timely detection can significantly impact patient outcomes. Beyond conventional bulk measurements, highly sensitive detection is also important for studying low-abundance biological processes and, ultimately, single-molecule events. Such measurements provide access to stochastic and transient phenomena that are often hidden in ensemble-averaged high-concentration measurements.

Among existing biosensing approaches, optical techniques are widely used due to their high sensitivity and versatility. In these systems, a biorecognition event is translated into a measurable optical signal, such as a change in light intensity, color, or refractive index [2], [3]. Fluorescence-based methods, in particular, can achieve extremely low detection limits and are commonly used in laboratory settings. However, they rely on external excitation sources and complex optical setups, which increases system cost, size, and operational complexity [4]. On the other hand, simple optical assays such as colorimetric lateral flow tests are inexpensive and user-friendly, but lack the sensitivity and quantitative capabilities of laboratory-based techniques [5].

This creates a gap between high-performance optical biosensing and practical POC deployment: current systems tend to offer either high sensitivity or high accessibility, but rarely both. This thesis explores an alternative biosensing approach that integrates bioluminescent signal generation with CMOS-based detection. In this framework, light is produced directly through a biochemical reaction, removing the need for external excitation and simplifying the optical design. In parallel, complementary metal–oxide–semiconductor (CMOS) image sensors provide a scalable, low-cost, and portable solution for detecting low-light signals. Together, these elements enable a user-friendly and accessible biosensing platform.

Particular focus was placed on understanding the intrinsic detection limits of the camera in order to determine the minimum photon levels that could be reliably and quantitatively measured. Another major objective was to maximize biosensor sensitivity at low analyte concentrations by identifying and employing a bright and stable bioluminescent system, and subsequently exploring signal enhancement strategies. At the same time, the work was motivated by the broader goal of developing approaches compatible with nanophotonic biosensing platforms investigated within the group. In this context, concepts inspired by fluorescence-based systems, including waveguiding semiconductor nanowire effects such as directional emission and digital detection schemes previously demonstrated in fluorescence-based platforms [6], [7], were considered as longer-term perspectives guiding this work.

The main outcomes of this thesis are as follows. First, we calibrated and evaluated a commercial CMOS camera sensor as a quantitative detector for scientific measurements, determining a usable dynamic range of approximately one order of magnitude around 10^4 photons/pixel under the experimental conditions used in this work. Second, we expressed and characterized a bioluminescent reporter system based on the NanoLuc enzymatic reaction. Third, we assembled and evaluated a complete bioluminescent CMOS-based biosensor platform and established its intrinsic detection limits under low-light and low-concentration conditions, achieving detection down to 10 nM, while at the same time using a separate microscopy-based reference setup. Finally, we demonstrated a proof-of-principle signal enhancement method called lock-in amplification method within the microscope setup, that could be compatible with the portable biosensor as well.

As is often the case in experimental research, the development of this work followed a non-linear and exploratory process. To present this clearly, the thesis is structured into three main chapters, each covering the theoretical and experimental foundations of a key component of the system. Chapter II focuses on the CMOS image sensor and its use as a quantitative light detector. Chapter III introduces the bioluminescent reporter system and its experimental characterization. Chapter IV presents the integrated sensing approach, including microscopy-based validation and signal enhancement concepts. Additional supporting investigations are included in the appendices, including studies of CMOS dark current and spatial resolution, an estimation of the NanoLuc detection threshold for camera sensitivity, and supplementary results from the signal enhancement, on bioluminescent signal decay. In the final section, we draw conclusions and discuss future directions.

II CMOS Camera-Based Optical Detection

II.1 Introduction to CMOS Cameras

Complementary Metal–Oxide-Semiconductor (CMOS) cameras are widely used in modern imaging systems, from smartphones and drones to medical devices and space applications [8]. Their popularity stems from their low cost; and low power consumption, leading to longer battery life, fast readout speed, and compatibility with standard electronic fabrication processes [9]. Taken together, the widespread use and low-cost fabrication of CMOS sensors make them well suited as the detector element for the biosensor in this work.

II.1.1 Anatomy of a CMOS Sensor

The simplest CMOS sensor pixel (3T) consists of a photodiode and three metal–oxide –semiconductor field-effect transistors (MOSFETs) [10]. This architecture enables each pixel to independently detect and process optical signals, effectively functioning as a complete optoelectronic unit. A three-dimensional representation of a CMOS pixel structure is shown in Fig. II.1a, where additional elements such as a micro-lens, which directs incoming light onto the photodiode and a color filter (in the case of color sensors) are included [11]. A complete CMOS sensor comprises an array of such pixels, typically arranged in a red–green–green–blue (RGGB) Bayer pattern, as shown in Fig. II.1b. This configuration is optimized for human visual perception, which is more sensitive to green wavelengths.

Finally, it is important to distinguish between a CMOS sensor and a CMOS camera. The sensor refers to the pixel array described above, whereas the camera denotes the complete system in which the sensor is integrated with supporting electronics, such as a circuit board and interfaces that enable communication with image acquisition software.

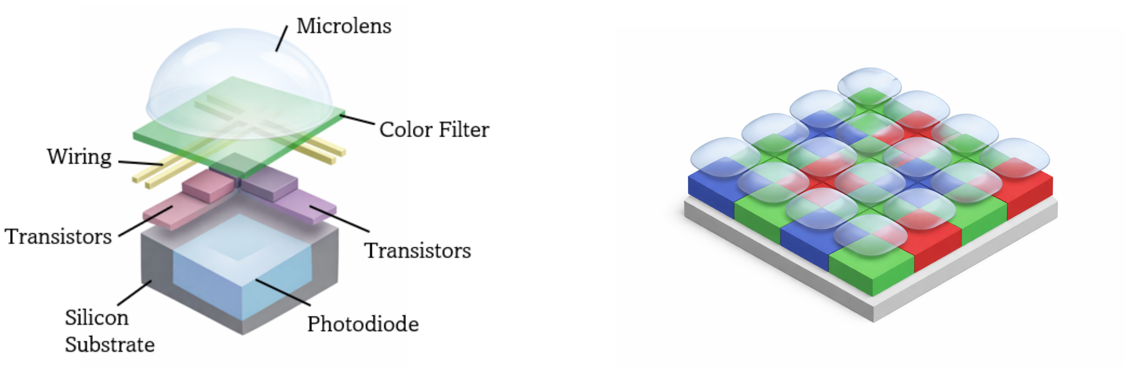

(a) (b)

Figure II.1: (a) Three-dimensional schematic of one fourth of a CMOS pixel [12] and (b) pixel array of a CMOS color sensor arranged in an RGGB Bayer pattern [13].

II.1.2 CMOS Sensor Linearity

In the context of a biosensor, the camera must operate as a quantitative detector of weak optical signals. Such quantitative analysis requires a clear understanding of the sensor's response, namely the relationship between the incident photon flux and the resulting digital output, which would ideally be linear. Since each pixel in a CMOS sensor functions as an independent detection and readout unit, the overall conversion process from incident photons to digital values can be described at the level of an individual pixel, as illustrated in Fig. II.2.

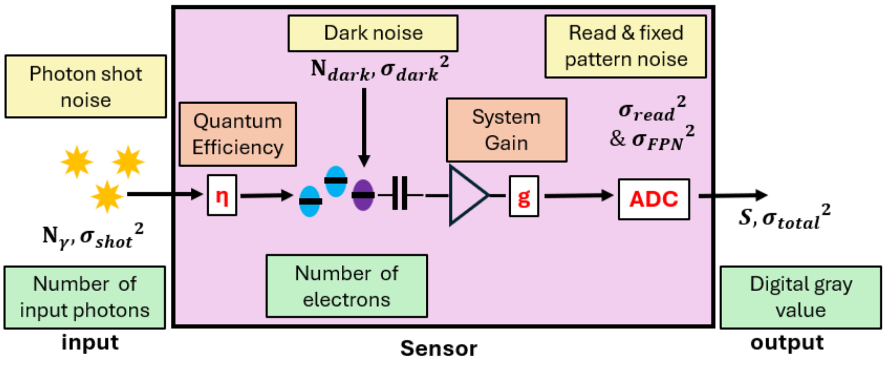

Figure II.2: Schematic illustration of the CMOS pixel workflow, inspired by [14]. Incident photons generate photoelectrons according to the sensor's quantum efficiency, with additional contributions from dark photoelectrons. The total charge is integrated, converted to a voltage via the pixel capacitance, amplified via system gain and digitized by an analog-to-digital converter (ADC) to produce a digital signal S with associated total variance σ^2.

When light reaches a CMOS pixel, the efficiency of the light-to-charge conversion process is described by the **quantum efficiency** (η), defined as the fraction of incident photons that are converted into collected electrons [15]:

$$\eta(\lambda) = \frac{N_e}{N_\gamma} = (1 - r) \ \cdot \zeta \ \cdot \left[1 - e^{-\alpha d}\right] \tag{II.1}$$

This expression reflects the successive stages of photodetection. The term $(1 - r)$ accounts for reflection losses r at the surface, $[1 - e^{-\alpha d}]$ describes the probability of photon absorption within the semiconductor (with absorption coefficient α and thickness d), and ζ represents the collection efficiency, accounting for carrier recombination losses. As a result, quantum efficiency is inherently wavelength-dependent.

Following the photon to electron convection, the accumulated charge is converted into a voltage, amplified, and finally digitized by an analog-to-digital converter (ADC). This overall process is assumed to be linear and can be described by a single parameter, the system gain K [Analogue to Digital Units (ADU)/e$^-$]. The system gain indicates how many digital units are produced for each detected electron [14]. The resulting digital signal is represented as a 16-bit value, giving an output range from 0 - 2^{16} ADU. The signal can therefore be expressed as:

$$S = K(N_e + N_{\text{dark}}) = S_{\text{dark}} + KN_e = K\eta N_\gamma \tag{II.2}$$

where N_{dark} represents the mean number of dark photoelectrons and $S_{\text{dark}} = KN_{\text{dark}}$ is the corresponding dark signal. In this context, the **responsivity** (R) is defined as [14]:

$$R(\lambda) = K \cdot \eta(\lambda) \tag{II.3}$$

Thus responsivity represents the effective conversion gain from photons to digital units (ADU/photon) and can be determined experimentally from the slope of the linear relationship between camera signal and the incident photon flux. This characteristic serves as the basis for assessing sensor linearity, thereby defining the effective operational range of the biosensor.

In practice, responsivity is the quantity most commonly specified by the manufacturer. In this work, the relative responsivity of the RGB CMOS sensor is shown in Fig. II.3, where the three curves correspond to the red, green, and blue channels of the camera.

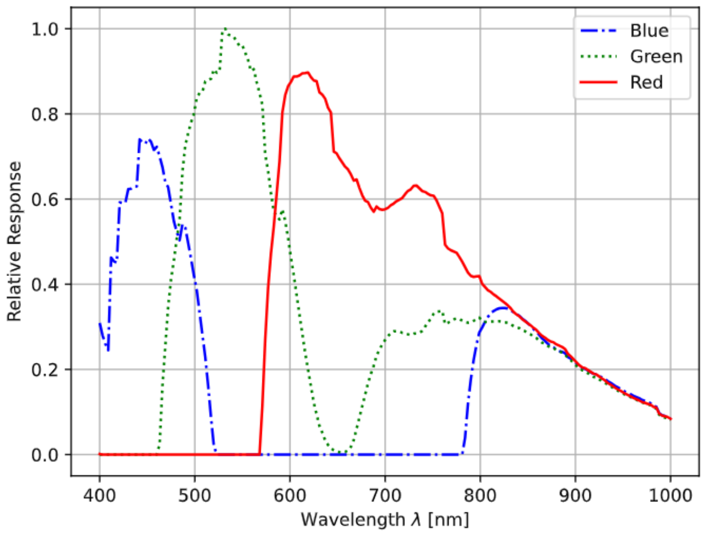

Figure II.3: Relative spectral responsivity of the RGB channels in a CMOS image sensor, normalized to the maximum response in green across all channels [16].

II.1.3 EXPERIMENTAL EXTRACTION OF CMOS LINEARITY AND RESPONSIVITY

We experimentally characterized the responsivity of the CMOS sensor by constructing a calibration curve relating the measured pixel signal to the number of incident photons. Figure II.4 (left part) shows the experimental setup. We illuminated the sensor with homogeneous LED light and recorded image series at increasing exposure times while keeping all other camera parameters constant. To account for the wavelength dependence of the sensor response, we used two LED sources with peak wavelengths of 525 nm (green) and 480 nm (blue).

For each exposure time, we extracted the average pixel signal S in ADU from the recorded images. We determined the corresponding number of incident photons per pixel from irradiance measurements performed using a power meter positioned at the same distance from the LED as the CMOS sensor, as shown in Fig. II.4 (right part). We then calculated the photon number per pixel during an exposure time t using:

$$N_{\text{photons}} = \frac{I\lambda}{hc} A_{\text{pixel}}\, t \tag{II.4}$$

where I is the measured irradiance, λ the LED wavelength, h Planck's constant, c the speed of light, and A_{pixel} the pixel area. For the sensor used in this work, $A_{\text{pixel}} = 2 \times 2\ \mu\text{m}^2$. The resulting calibration curve of average pixel intensity versus incident photons determines both the linear operating range of the sensor and its slope the responsivity.

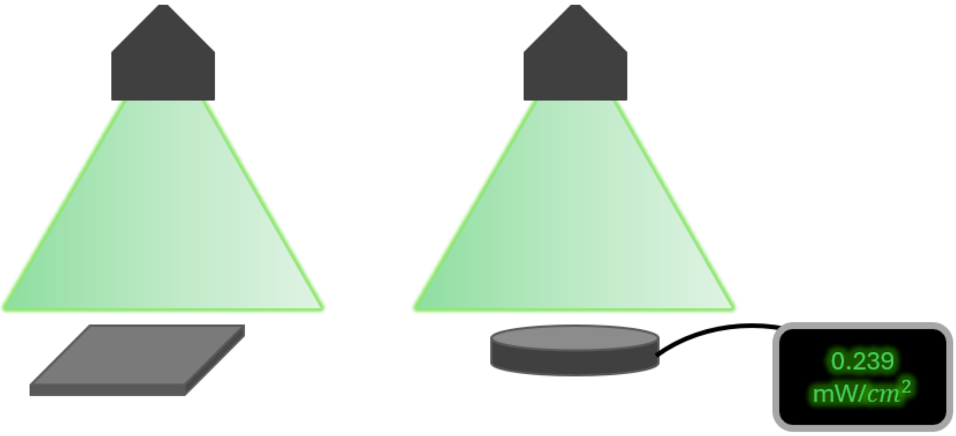

Figure II.4: Left: Homogeneous LED illumination of the CMOS sensor during calibration measurements. Right: Irradiance measurement setup using a calibrated power meter.

II.1.4 LIMITS OF THE LINEAR MODEL (NOISE FLOOR AND SATURATION)

The aforementioned calibration curve is not linear over the full measurement range, but is instead limited at both low and high photon counts. To begin with, a CMOS pixel cannot store an unlimited number of photoelectrons. The maximum charge it can hold is defined by the **full well capacity**. Once this limit is reached, the pixel saturates and the output signal no longer linearly increases with incident photons, thereby setting the upper bound of the sensor's dynamic range.

At low signal levels, the sensor response is limited by noise contributions, which define the lower bound of the dynamic range. These noise sources can be broadly categorized into fundamental (statistical) and device-related (electronic) contributions [17]. In this work, the noise is first described in terms of the number of detected photoelectrons N, reflecting the underlying physical processes, and can be converted to digital units S [ADU] via the system gain.

The most fundamental contribution is **photon shot noise** (σ_{shot}), arising from the stochastic arrival of photons and following Poisson statistics:

$$\sigma_{\text{shot}} = \sqrt{N} \quad \text{or} \quad \sigma_{\text{shot}} = \sqrt{S}. \tag{II.5}$$

A second fundamental source is **dark current noise** (σ_{dark}), caused by thermally generated charge carriers:

$$N_{\text{dark}} = D \cdot t, \quad \sigma_{\text{dark}} = \sqrt{N_{\text{dark}}} \quad \text{or} \quad \sigma_{\text{dark}} = \sqrt{S_{\text{dark}}} \tag{II.6}$$

The dark current rate D increases with temperature according to:

$$D \propto e^{-E_g/(kT)} \tag{II.7}$$

making it particularly relevant for long exposure times [18]. In addition, **read noise** (σ_{read}) is introduced during charge-to-voltage conversion and digitization. It is largely signal-independent and can be treated as a constant:

$$\sigma_{read} = \text{const} \tag{II.8}$$

Finally, **fixed pattern noise** (σ_{FPN}) arises from pixel-to-pixel variations and scales with the signal:

$$\sigma_{\text{FPN}} = \alpha S \tag{II.9}$$

where $\alpha \ll 1$ [19]. Assuming these contributions are independent, the total noise is given by:

$$\sigma^2_{\text{total}} = \sigma^2_{\text{shot}} + \sigma^2_{\text{dark}} + \sigma^2_{read} + \sigma^2_{\text{FPN}} \tag{II.10}$$

Overall, while photon shot noise sets the fundamental limit, read and dark noise often dominates in low-light biosensing applications.

Signal Treatment and Noise Mitigation

The recorded pixel value S includes both the desired signal and background contributions (e.g., ambient light) as well as noise. To isolate the relevant signal, a background image S_{bg} is acquired under identical conditions without the signal of interest. The corrected signal is then:

$$S_{\text{corr}} = S - S_{\text{bg}} \tag{II.11}$$

This procedure removes ambient light and the mean dark signal, and reduces fixed pattern noise. However, stochastic components such as photon shot noise remain. To ensure statistical significance, a threshold criterion is applied:

$$S_{\text{corr}} \geq 3\sigma \tag{II.12}$$

where σ is the standard deviation determined using ImageJ. This 3σ threshold is commonly used under the assumption of approximately Gaussian noise. It should be noted that real sensors may exhibit deviations from ideal Gaussian behavior due to effects such as hot pixels, which can lead to increased false positives or the rejection of weak signals near the detection limit [20, 21].

II.2 THE BASLER (DAA3840-45UC) CAMERA MODEL

This thesis uses a Basler daA3840-45uc color (RGB) camera, which is equipped with a Sony IMX334 CMOS sensor [16]. The following subsections provide an overview of the key hardware and software components involved in the image acquisition process.

II.2.1 Hardware Configuration

The Basler daA3840-45uc camera module is a compact board-level device integrating a CMOS image sensor, readout electronics, and external interfaces. The module was originally equipped with an S-mount lens holder, allowing the attachment of standard S-mount lenses (Fig. II.5a). For the purposes of this work, the mount was mechanically removed to enable direct access to the sensor area.

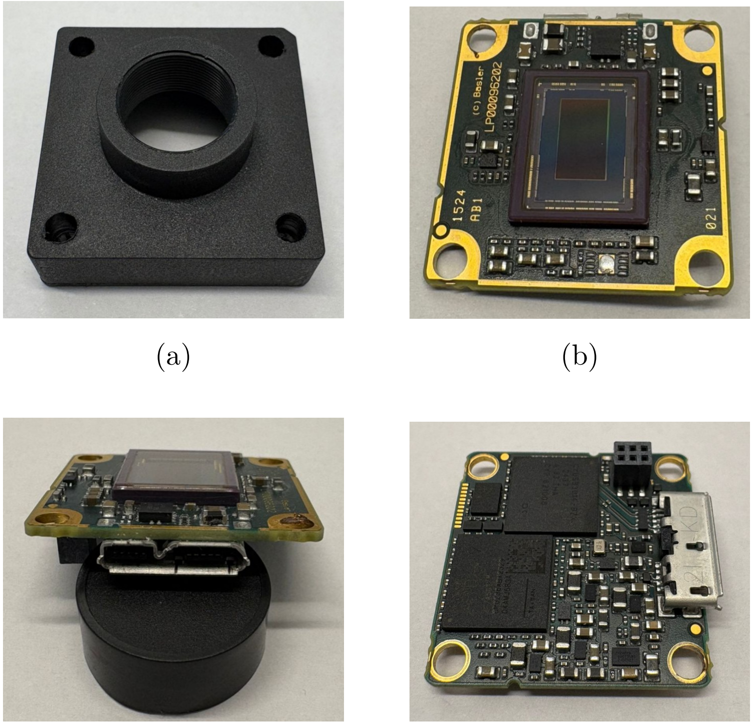

(a) (b)

(c) (d)

Figure II.5: Photos of the Basler daA3840-45uc camera module from different perspectives. (a) Removed S-mount. (b) Top view showing the sensor and PCB. (c) Side view showing the USB interface. (d) Bottom view showing the status LED.

Additional views of the camera module are shown in Fig. II.5b–II.5d. Figure II.5b highlights the location of the sensor area together with the surrounding electronics. The sensor chip is enclosed within a protective package topped with a transparent cover glass. In the context of this thesis, the presence of this glass is particularly important, as it introduces a finite distance between the object and the pixels, thereby affecting the spatial resolution, as discussed in later sections. Figure II.5c shows the external USB 3.0 Micro-B interface, which provides both power delivery and data communication between the camera and the computer. Finally, Fig. II.5d reveals additional electronic components together with a status LED that illuminates when the device is connected. During low-light measurements, this LED was identified as a major source of unwanted background illumination and was therefore deactivated by setting the device indicator mode parameter to inactive.

II.2.2 SOFTWARE CONTROL AND IMAGE ACQUISITION

Image acquisition and camera control were performed using the *Basler pylon Software Suite* [22], which provides both a graphical interface (pylon Viewer) and programmatic access to camera parameters.

As shown in Fig.II.6, the interface is divided into several main components: device selection, image display, and parameter control. The camera is selected from the list of connected devices, after which acquisition parameters can be configured in the feature panel. The software enables real-time monitoring of captured images and provides access to both basic and advanced camera settings. For this work, we operated the camera in a configuration optimized for quantitative measurements rather than visual image enhancement. In particular, we disabled all automatic image processing features to ensure that the recorded pixel values remained directly proportional to the detected photon flux. The following parameters were of primary importance:

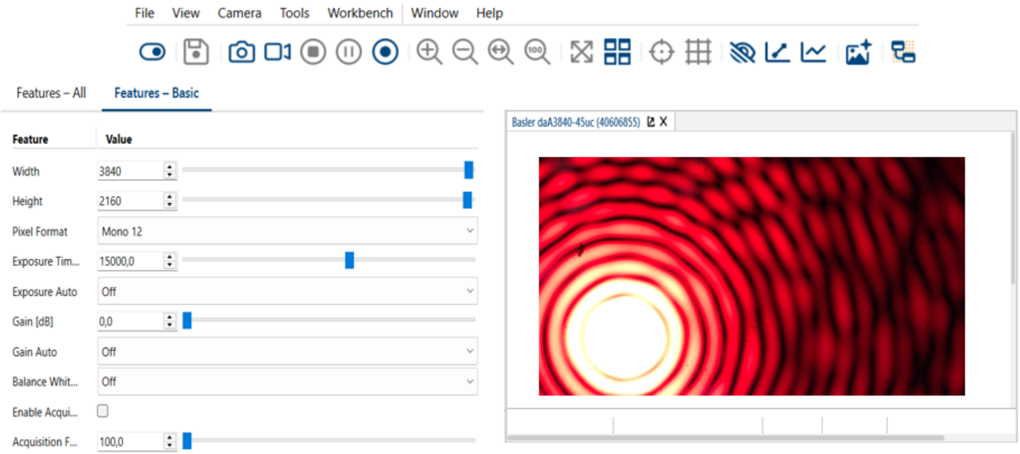

Feature	Value
Width	3840
Height	2160
Pixel Format	Mono 12
Exposure Tim...	15000,0
Exposure Auto	Off
Gain [dB]	0,0
Gain Auto	Off
Balance Whit...	Off
Enable Acqui...	☐
Acquisition F...	100,0

Figure II.6: Pylon Viewer software interface. The workbench is shown at the top, image acquisition parameters are displayed on the left, and the image panel on the right shows a red laser pointer source.

- **Pixel format:** We operated the camera in Mono12 mode to preserve a high dynamic range and avoid artifacts associated with color interpolation. In addition, we used a Mono16 format, in which the 12-bit sensor data were mapped into a 16-bit container to improve compatibility with image-processing pipelines.

- **Exposure time:** We operated the camera using manual exposure, as exposure time constituted the primary control parameter over the acquired signal. For this camera, we used exposure times ranging from 51 μs to 1 s.

- **Gain:** We fixed the user-adjustable analog gain at 0 dB (G=1) to avoid additional signal amplification and preserve a direct proportional relationship between the detected photoelectrons and the recorded digital signal. The intrinsic conversion gain K of the CMOS sensor (as defined in Section II.1.2) and the associated readout noise contributions remain and are determined by the sensor architecture itself.

- **Gamma correction:** We set the gamma correction to 1, corresponding to the linear case of the power-law transformation $I_{\text{out}} = I_{\text{in}}^{\gamma} = I_{\text{in}}$, in order to maintain proportionality between the recorded pixel intensity and the incident light intensity [23].

II.3 CMOS Reference Microscopy System

This section introduces the optical microscopy setup that we used as a reference system for comparison with the CMOS camera measurements. For the purposes of this thesis, we operated the microscope in both brightfield and fluorescence imaging modes. Optical microscopy relies on lenses and visible light to magnify and resolve structures that are otherwise invisible to the naked eye. In both imaging modes, the microscope objective collected light from the sample and projected an image onto a CCD camera for digital acquisition.

II.3.1 Brightfield Mode

Brightfield microscopy is one of the simplest and most widely used optical imaging techniques. In this mode, the sample is illuminated with broad-spectrum white light. The light is focused onto the sample by a condenser lens, while the transmitted light is collected by an objective lens positioned below the sample and guided to the camera. Regions of the sample that absorb or scatter light appear darker than the surrounding background, which remains bright, hence the term bright field. This difference in transmitted intensity produces the image contrast. A simplified schematic of the brightfield microscopy setup is shown in Figure II.7a.

II.3.2 Fluorescence Mode

Fluorescence microscopy enables imaging of specific structures within a sample by detecting light emitted from fluorescent molecules (fluorophores) attached to them. In this imaging mode, the sample is illuminated with excitation light of a specific wavelength, typically provided by a laser or LED source. The fluorophores absorb the excitation light and subsequently emit light at longer wavelengths through the process of fluorescence. The optical setup includes an excitation filter, a dichroic

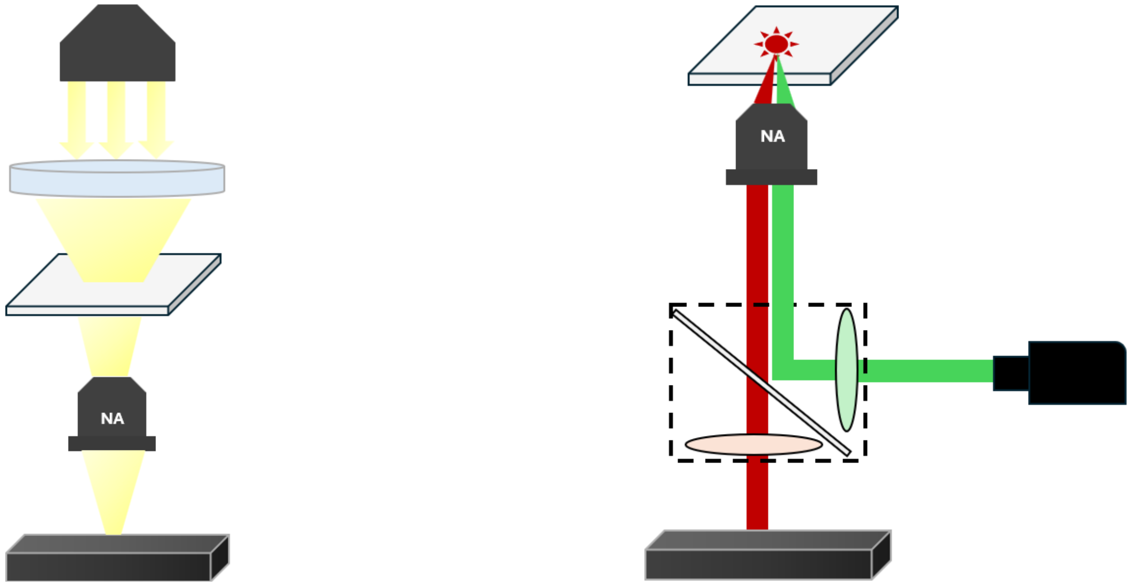

(a)

(b)

Figure II.7: Schematics of optical configurations used for (a) brightfield microscopy and (b) fluorescence microscopy.

mirror, and an emission filter, which together form the filter cube. The excitation filter selects the desired illumination wavelength before the light is reflected by the dichroic mirror toward the sample through the objective lens. The emitted fluorescence is then collected by the same objective lens, passes through the dichroic mirror and emission filter, and is finally detected by the camera.

This filtering arrangement efficiently separates the excitation and emission light, allowing primarily the fluorescence signal to reach the detector. As a result, fluorescence microscopy provides high image contrast and molecular specificity, enabling selective visualization of labeled structures within complex biological samples. Many of these structures are typically invisible in conventional brightfield microscopy. A simplified schematic of the fluorescence microscopy setup is shown in Figure II.7b.

III BIOLUMINESCENCE

As discussed in the thesis, a biosensor integrates a biological recognition element with a physical transducer [24]. The previous chapter described the transduction mechanism, implemented using an optoelectronic CMOS detector. This chapter focuses on the biological recognition element, which in this work is based on bioluminescence.

III.1 INTRODUCTION TO BIOLUMINESCENCE

Bioluminescence is a natural phenomenon observed in a wide range of organisms, including bacteria, fungi, insects such as fireflies, and numerous marine species. Some examples are illustrated in Fig.III.1. Bioluminescence arises from a biochemical reaction in which a specific light-emitting substrate (luciferin) is oxidized by an enzyme catalyst (luciferase), resulting in the emission of photons. Luciferins are commonly used to classify bioluminescent systems, as each luciferase is typically specific to each organism. The main groups include beetle D-luciferin, marine coelenterazine (CTZ), and bacterial and fungal luciferins [25].

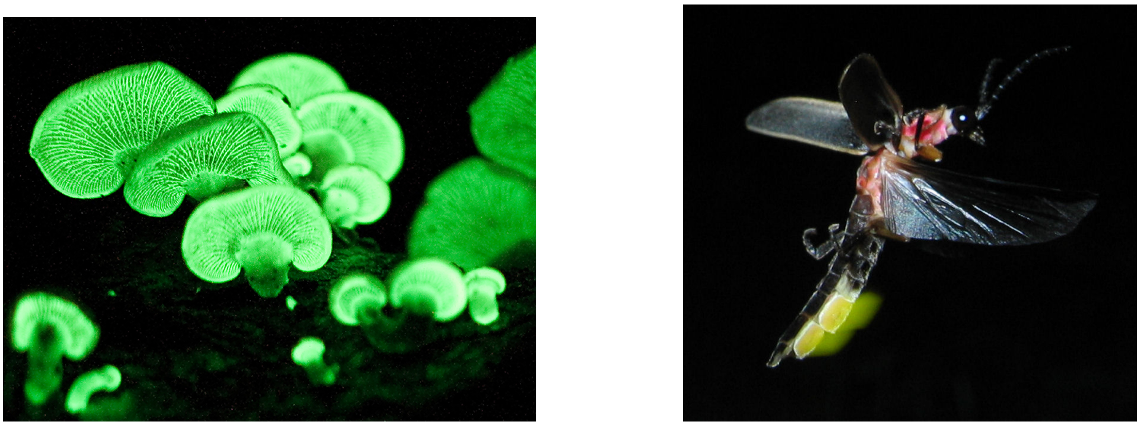

(a)

(b)

Figure III.1: Examples of bioluminescence in nature. (a) The fungus *Panellus stipticus* [26]. (b) The firefly *Photinus pyralis* [27].

This naturally occurring process has been widely harnessed for analytical and sensing applications, particularly in label-free live-cell studies [28]. In such contexts, bioluminescent systems are adapted into reporter assays, that convert biological activity into measurable light signals. Compared to fluorescence, which together with bioluminescence are the two dominant luminescence-based imaging modalities in current research, the latter offers several key advantages:

- **Low Noise:** The light is generated intrinsically by the biochemical reaction, eliminating the need for external illumination and thereby avoiding excitation-induced background, scattered light, optical crosstalk, and autofluorescence. As a result, bioluminescent assays often provide a superior signal-to-noise ratio in complex biological samples.

- **Improved imaging depth:** The absence of excitation light is particularly advantageous for imaging in scattering media such as tissue, where external illumination in fluorescence microscopy can limit penetration depth and reduce contrast.

- **Non-invasive readout:** In many applications, bioluminescence enables measurement without physically perturbing the sample. In addition, the reagents are generally biocompatible and non-radiative, which makes this approach especially valuable for longitudinal studies in cells, tissues, and small animal models.

- **Minimal photobleaching:** In fluorescence-based systems, the target molecule is labeled with a fluorophore that gradually loses its ability to emit light under continuous excitation, typically within minutes due to photobleaching. In contrast, bioluminescent systems label the target with a luciferase enzyme rather than the light-emitting molecule itself. As long as substrate is continuously supplied, the enzymatic reaction can sustain light emission for several hours, enabling significantly longer observation times.

Despite these advantages, bioluminescence also has an important limitation. In contrast to fluorescence, where continuous external excitation can generate high photon flux, reaching $10^6 - 10^8$ photons per second [29], bioluminescent emission is limited by enzyme kinetics, resulting in photon output that is several orders of magnitude lower on a per-molecule basis [30]. As a result, the emitted signals are inherently weaker, which can limit temporal resolution and place stringent requirements on detection sensitivity, particularly when using standard imaging hardware such as CMOS sensors. This trade-off between low background and low signal intensity is central to the design challenges addressed in this work. In particular, the need to reliably detect weak bioluminescent signals motivates the development of signal enhancement strategies and optimized detection approaches, as explored in the next chapter of this thesis.

Recent research in bioluminescence has primarily focused on three main directions: (i) enhancing luciferase brightness and stability through protein engineering [31], (ii) developing genetically encoded biosensors for monitoring intracellular analytes and signaling [32], and (iii) extending bioluminescent readouts to imaging platforms and portable detection systems [33]. This thesis falls within the third category and employs the engineered luciferase NanoLuc.

III.2 NanoLuc Luciferase

NanoLuc luciferase is a small (19 kDa) enzyme derived from the deep-sea shrimp *Oplophorus gracilirostris*. It was developed through protein engineering and substrate optimization to provide enhanced temperature and pH stability, extended signal half-life, and significantly increased luminescence output, up to 150 times higher than conventional luciferases [34]. More specifically, under saturating substrate conditions, each enzyme molecule can produce on average 8.6 photons per second [35].

The bioluminescence reaction of interest is the oxidation of the substrate furimazine under NanoLuc catalysis, producing furimamide, carbon dioxide, and blue light with a peak emission at 460 nm, as can be seen in Fig. III.2.

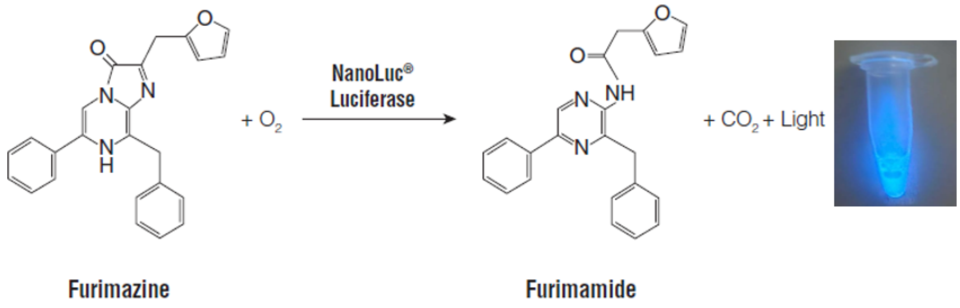

Figure III.2: The bioluminescent reaction catalyzed by NanoLuc luciferase with a real image of the resulting light in solution.

For the purposes of this thesis, the substrate (furimazine) is assumed to be present in excess throughout the reaction. Under these conditions, the emitted light intensity is primarily governed by the concentration of luciferase, enabling a direct relationship between enzyme concentration and optical signal output.

In practice, the substrate is commercially available and prepared according to the manufacturer's instructions by mixing Nano-Glo® Luciferase Assay Substrate with

Nano-Glo® Luciferase Assay Buffer at a ratio of 1:50 [36]. In contrast, NanoLuc luciferase is expressed from scratch in the laboratory.

III.3 PROTEIN EXPRESSION AND CHARACTERIZATION

This section provides a brief overview of the methodological aspects of protein expression and handling in the biochemistry laboratory, presented from and for a physicist's perspective, with emphasis on the principles relevant to this work rather than detailed biochemical protocols. The procedures described below follow the specific laboratory protocols used in this work, which may vary in implementation and optimization between laboratories, although the underlying methodological principles are generally common across standard protein expression workflows.

III.3.1 PROTEIN EXPRESSION IN *E. COLI*

Protein expression begins with the design of a golden gate plasmid, a small circular DNA molecule that functions as an instruction set for the bacteria. It carries the gene of interest together with regulatory elements that control when protein production is switched on, as well as a short affinity tag (His_6) that later allows the protein to be selectively purified.

This plasmid is introduced into *E. coli* cells through a process known as heat shock. The bacteria are first chemically treated to make their membranes more permeable, and then briefly exposed to elevated temperature. This sudden temperature change creates a transient opening in the cell membrane, allowing the plasmid DNA to enter before the membrane reseals. Only a fraction of the cells successfully take up the plasmid, so the culture is grown in the presence of an antibiotic. Since the plasmid also carries an antibiotic resistance gene, only the bacteria that have incorporated the plasmid survive and continue to grow.

The transformed bacteria are then cultivated in a nutrient-rich medium (Lysogeny Broth), which provides the necessary resources for rapid growth and division. As the bacterial population increases, each cell replicates the plasmid and therefore retains the instructions for protein production. At a suitable cell density, expression of the target protein is induced,by adding IPTG (isopropyl β-D-1-thiogalactopyranoside), which activates the transcriptional machinery encoded on the plasmid. From this point onward, the bacteria effectively act as microscopic production units, synthesizing large amounts of the desired protein over several hours.

After sufficient expression, the cells are harvested by centrifugation and subsequently lysed by sonication to release their intracellular contents. This results in a complex mixture containing the target protein alongside many other cellular components. To isolate the protein of interest, immobilized metal affinity chromatography (IMAC) is used. The His_6-tag on the protein binds selectively to nickel ions immobilized on a resin, allowing the target protein to be retained while most other components are washed away. The protein is then eluted by adding imidazole, which competes for binding to the nickel sites, thereby releasing the purified protein from the column.

A simplified schematic overview of the protein expression workflow is shown in Figure III.3.

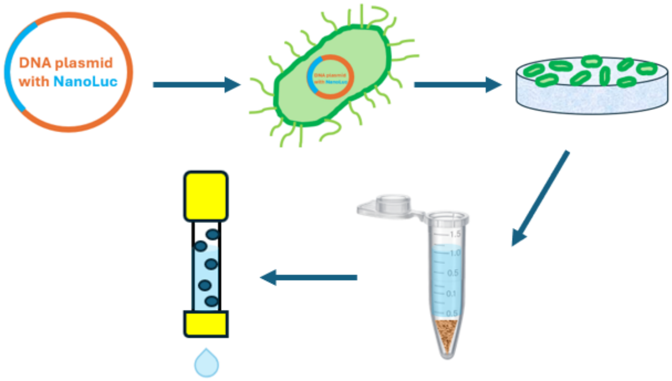

Figure III.3: A plasmid containing the NanoLuc gene is first constructed and subsequently transformed into *E. coli*. The transformed cells are grown in LB plates. After expression, cells are lysed, yielding a mixture in which cellular debris forms a pellet at the bottom of an eppendorf tube, while the soluble protein remains in the supernatant. The target protein is then isolated using IMAC purification.

III.3.2 Protein Concentration

Protein concentration is determined using NanoDrop UV–Vis spectroscopy. This technique measures the absorbance of a small-volume sample at 280 nm, where proteins absorb due to aromatic amino acids such as tryptophan and tyrosine [37]. The concentration is calculated using the Beer–Lambert law:

$$A = \varepsilon\, c\, l \tag{III.1}$$

where A is the measured absorbance (unitless), ε is the molar extinction coefficient ($\mathrm{M^{-1}\,cm^{-1}}$), describing how strongly a substance absorbs light at a given wavelength, c is the molar concentration (M), and l is the optical path length (cm). So by measuring absorbance at 280 nm, the protein concentration can be calculated, when the molar extinction coefficient is known.

Although protein concentration is commonly expressed in mass units (mg/mL), molarity ($\mathrm{mol\,L^{-1}}$) is more relevant for biosensing applications, as it reflects the number of molecules in solution and therefore governs molecular interactions, enabling quantitative and comparative analysis.

For completeness, conversion from mass concentration to molarity requires the molecular weight of the protein, typically given in kilodaltons (kDa), where 1 kDa = 1000 g/mol. The relationship is given by:

$$c = \frac{\text{concentration (mg/mL)}}{\text{molecular weight (kDa)}} \times 10^3 \tag{III.2}$$

yielding c in $\mathrm{mol\,L^{-1}}$.

III.3.3 Protein Size and Purity

Protein size and purity were assessed using sodium dodecyl sulfate polyacrylamide gel electrophoresis (SDS–PAGE). This technique separates proteins primarily based on their molecular weight. For this technique, proteins are first treated with the detergent sodium dodecyl sulfate (SDS), which denatures them and unfolds them into extended chains. At the same time, SDS binds uniformly along the polypeptide backbone, imparting a nearly constant negative charge per unit length. As a result, differences in the native shape and charge of proteins are minimized, and their migration through the gel depends predominantly on their molecular weight.

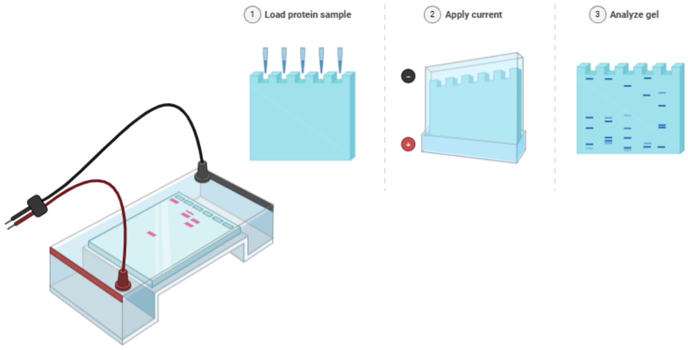

Figure III.4: Protein samples and ladders are loaded into wells at the top of a polyacrylamide gel, and an electric field is applied across the gel. Negatively charged proteins migrate vertically toward the positive electrode, with smaller proteins moving faster through the gel matrix. After electrophoresis, the gel is analyzed by visualizing the resulting band pattern.This figure was made in BioRender.com.

The protein samples, along with molecular weight marker ladders, are loaded into a polyacrylamide gel and an electric field is applied. The negatively charged proteins migrate toward the positive electrode, with smaller proteins moving more easily through the porous gel matrix and therefore traveling faster than larger ones. Although this separation is commonly described in terms of "size," it is fundamentally determined by molecular weight (typically reported in kDa). Under these denaturing conditions, proteins are unfolded and adopt similar shapes, meaning their migration through the gel depends primarily on molecular mass, which in turn correlates with their effective size.

After electrophoresis, the proteins are visualized using staining with Coomassie Blue. The position of the bands is compared to the molecular weight ladder control to estimate protein size, while the number and intensity of bands provide information about sample purity. A schematic of the electrophoresis workflow is shown in Fig.III.4.

III.4 Binding of Luciferase to Surfaces

In this thesis, some experiments involve the immobilization of luciferases onto solid substrates such as nanowires and glass slides. To achieve controlled and specific binding, an engineered protein system was designed and expressed. The luciferase construct is fused to a SpyTag3 peptide, while a second protein consisting of bovine serum albumin (BSA) fused to SpyCatcher3 was expressed separately. The BSA component forms a coating on the target surface, effectively functionalizing it, while the SpyTag3–SpyCatcher3 system enables specific and covalent coupling of the luciferase to the surface. Upon interaction, SpyTag and SpyCatcher spontaneously form a covalent isopeptide bond, resulting in a stable and irreversible linkage [38]. An improved third-generation variant (SpyTag3/SpyCatcher3) exhibits enhanced reaction kinetics and performance [39]. This mechanism allows for site-specific immobilization of luciferase while minimizing nonspecific binding. A schematic illustration of the binding mechanism on a glass slide is shown in FigIII.5.

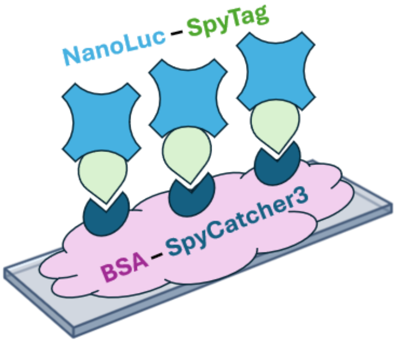

Figure III.5: Schematic illustration of intended luciferase immobilization on a glass surface via the SpyTag3–SpyCatcher3 system.

To verify protein expression and assess binding, we performed SDS–PAGE on the individually expressed proteins (NanoLuc–SpyTag3 and BSA–SpyCatcher3), along with a separate lane containing a mixture of the two. If both proteins are functional, they should bind in solution, producing a band corresponding to the combined molecular weight of the two constructs. For clarity it is worth noting, that the schematic depicts the intended mechanism, however in this work the binding system could not be experimentally demonstrated due to poor BSA-SpyCatcher3 expression.

IV Engineering the Device

Having described the two primary components of the biosensor, namely the optical detection system and the bioluminescent signaling mechanism, this chapter focuses on their integration into a functional device. Following the device construction, we evaluate its performance through initial control experiments and the investigation of signal enhancement techniques. Together, this chapter outlines the transition from individual components to an operational sensing platform and establishes the foundation for its characterization, performance assessment, and further optimization.

IV.1 Device Design and Fabrication

To mechanically integrate the camera chip with the bioluminescent system, we employed low-cost and easily accessible fabrication methods. The device consists primarily of two custom 3D-printed components. First, we designed a square base (Fig. IV.1a) to support the camera module from below. This base ensures that the sensor surface remains level by compensating for the tilt introduced by the USB interface, thereby improving alignment and measurement consistency.

Second, we fabricated a custom-designed enclosure cap and placed it over the camera chip (Fig. IV.1c). The cap isolates the system from external illumination and environmental noise. The choice of white material provides partial reflectivity: it reduces the impact of incoming ambient light while also reflecting a portion of the emitted bioluminescent signal back toward the sensor. In principle, this slightly increases the light collection efficiency by broadening the effective acceptance angle.

Finally, we fabricated and positioned a rectangular PDMS well directly on top of the active sensing area of the camera chip. Polydimethylsiloxane (PDMS) is widely used in microfluidics and bioanalytical applications due to its optical transparency, biocompatibility, and ease of fabrication [40]. In this design, the PDMS structure (Fig. IV.1b) serves a dual purpose. First, it confines liquid samples, preventing them from spreading onto surrounding electronics and causing damage. Second, its geometry constrains the shape of the bioluminescent droplet. In the absence of such confinement, droplets would naturally form a spherical cap, which can introduce optical lensing effects. This lensing may focus background light and artificially increase the noise floor. The rectangular geometry mitigates this effect, thereby contributing to more stable and reliable signal measurements.

(a) 3D printed camera base (b) fabricated PDMS well

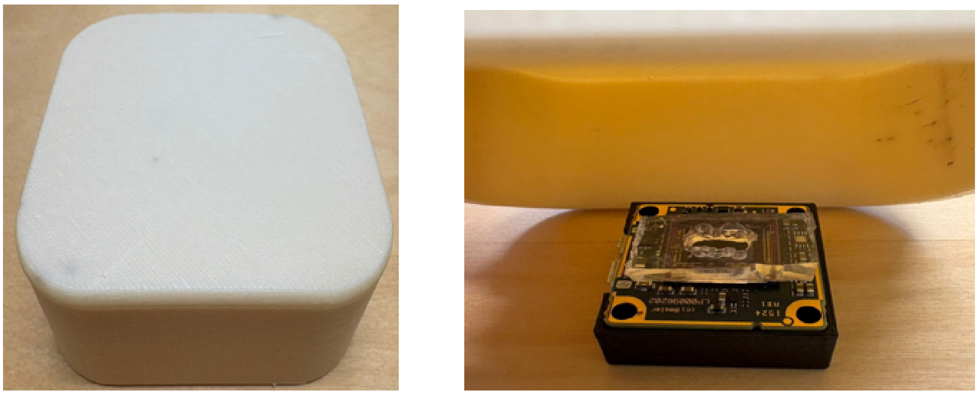

(c) 3D printed white cap (d) Full device setup

Figure IV.1: Photographs of individual components of the biosensing device, as well as the complete assembled system with the cap on top slightly tilted.

The fully assembled device, as used in the experiments, is depicted in Fig. IV.1d.

IV.2 Baseline Bioluminescence Measurements

After assembling the device, we performed baseline bioluminescence experiments using the NanoLuc luciferase system. Building on the camera calibration measurements described in Section II.3.1, we mapped the experimentally generated bioluminescent signals onto the corresponding photon-count calibration plots in order to evaluate the intrinsic detection capability of the developed platform prior to introducing signal enhancement strategies.

We mixed a NanoGlo substrate solution, prepared as described in Section III.2, with NanoLuc luciferase initially diluted to 1 µM, corresponding to relatively high signal conditions compared to typical single-molecule biosensing experiments. We selected this starting concentration based on the theoretical estimations presented in Appendix C. We then introduced the resulting bioluminescent solution into the PDMS well positioned directly above the camera sensor, as depicted in Fig. IV.2a.

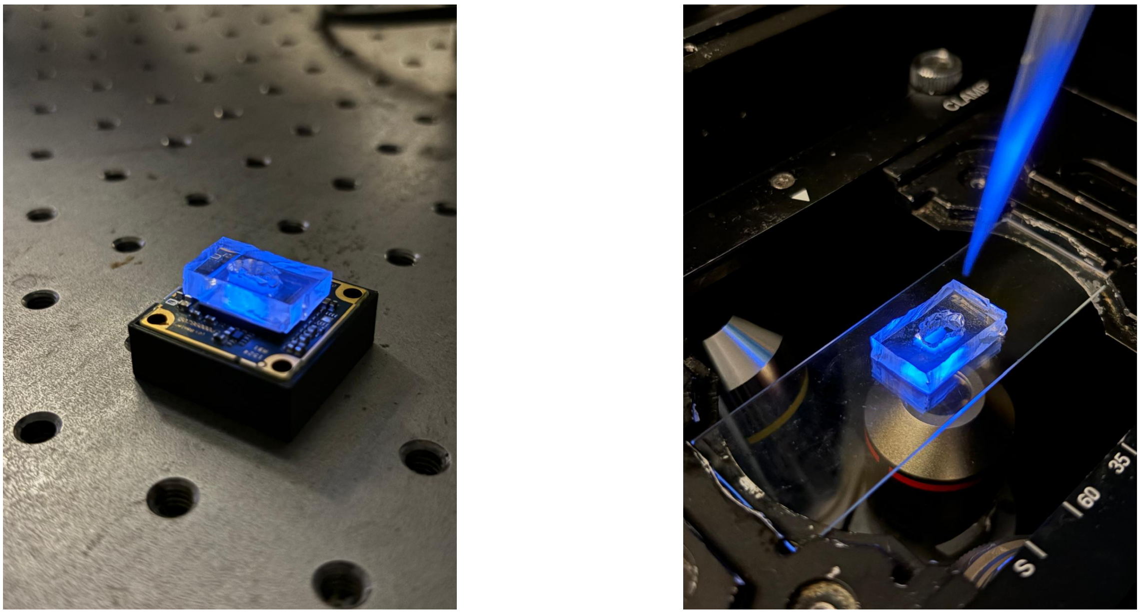

(a) (b)

Figure IV.2: Real images of control bioluminescence based experiments. (a) camera-based device with the PDMS well positioned directly above the CMOS sensor. (b) microscopy-based setup used as a reference detection system.

Once we confirmed signal detection, we progressively reduced the NanoLuc concentration in order to estimate the minimum enzyme concentration capable of producing a measurable signal. During these measurements, we systematically adjusted the camera exposure time to optimize signal detection under low-light conditions. In addition, we applied temporal integration over multiple acquired images to improve the signal-to-noise ratio.

To provide a reference measurement, we performed the same dilution series and experimental procedure using the microscopy-based detection setup shown in Fig. IV.2b. We carried out the measurements in a brightfield configuration with the illumination source switched off, such that the only detected light originated from bioluminescence. These microscopy measurements, enabled a direct comparison between the performance of the developed camera-integrated biosensor platform and that of a conventional laboratory imaging system.

IV.3 SIGNAL ENHANCEMENT

In highly sensitive biosensing systems, particularly when approaching low concentration or single-molecule detection regimes, the intrinsic signal generated by the assay is often comparable to or smaller than the background noise of the detection system. As a result, the detector performance alone is often insufficient, and additional signal enhancement strategies are required to improve sensitivity. A wide range of enhancement approaches have therefore been developed in optical biosensing. Examples include enzymatic amplification, where a single target molecule initiates the production of many detectable products [41], plasmonic enhancement using metallic nanostructures to locally enhance optical fields and increase signal intensity [42] and post-processing approaches such as wavelet denoising, a mathematical filter for suppressing stochastic noise contributions in recorded signals [43].

IV.3.1 LOCK-IN AMPLIFICATION THEORY

The signal enhancement approach investigated in this work is based on lock-in amplification, a post-acquisition signal processing technique widely used in optoelectronics to extract weak periodic signals from noisy backgrounds [44]. In lock-in amplification, the measured time-domain signal $s(t)$ is analyzed relative to a known reference modulation frequency by transforming the signal into frequency space using the Fourier transform:

$$S(f) = \int_{-\infty}^{\infty} s(t)\, e^{-i2\pi f t}\, dt \tag{IV.1}$$

where $s(t)$ is the signal in the time domain, f is the frequency, and $S(f)$ represents the spectral content of the signal in frequency space. After Fourier transformation, signal components oscillating at the reference frequency appear as narrow peaks in the frequency spectrum, while most noise sources, such as shot noise, thermal noise, and electronic read noise, remain broadly distributed across frequencies. This frequency selectivity enables weak periodic signals to be distinguished even when they are difficult to identify directly in the time domain.

This approach is particularly attractive for bioluminescence-based biosensing. In such systems, the luciferase enzyme can remain present within the field of view, while light emission only occurs upon introduction of the substrate. By periodically modulating the substrate delivery, the emitted optical signal can in principle be switched on and off at a controlled frequency and without photo bleaching, thereby generating a characteristic spectral signature that can be isolated from background noise.

IV.3.2 Frequency Entraining Experimental Implementation

We experimentally investigated the lock-in amplification concept using a microfluidic device on the microscope platform. Due to challenges associated with immobilizing luciferase inside the channel within the time frame of this project, we used fluorescein instead as a model fluorescent system. The microfluidic device consisted of two outlet and three inlet channels connected to a common imaging region, as shown in Fig.IV.3.

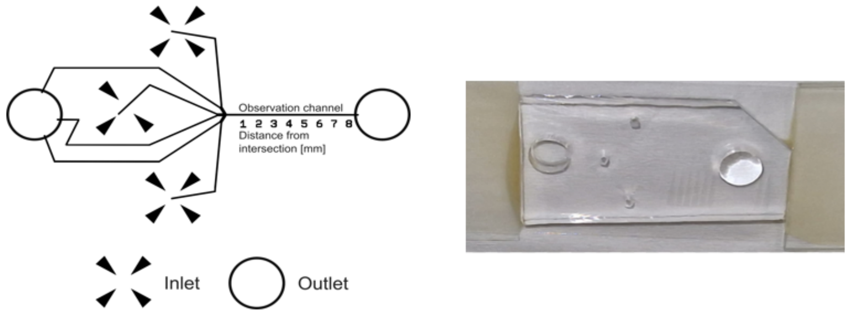

Figure IV.3: Left schematic illustration the microfluidic device, consisting of 3 inlets and 2 outlets. Right real image of the device.

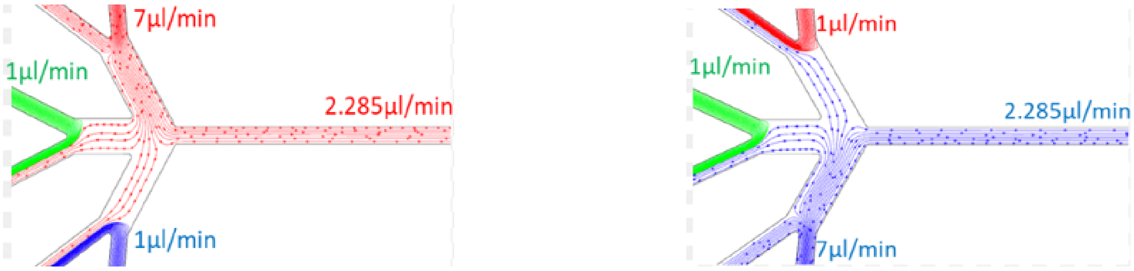

(a)

(b)

Figure IV.4: Simulation of microfluidic channels modulation. (a) With red color PBS flowing through the imaging region, corresponding to the “off” state. (b) With blue color fluorescein flowing through the imaging region, corresponding to the “on” state.

We used the top and bottom inlet channels for alternating delivery of phosphate-buffered saline (PBS), corresponding to the “off” state, and fluorescein solution, corresponding to the “on” state, as illustrated in Figures IV.4a and IV.4b respectively. We achieved modulation by controlling the relative inlet flow rates, driving the channel occupying the imaging region at 7 µL/min while maintaining the remaining channels, including the third inlet from a previously existing laboratory design [45], at 1 µL/min to preserve a stable flow profile. We investigated modulation periods of 200 ms and 500 ms to match the exposure times used in the bioluminescence experiments described in Section IV.2.

V Results

V.1 Camera chip calibration

In this subsection, we present the main results of the camera chip calibration described in Subsection II.3.1. The calibration curves shown in Fig. V.1 display the average pixel signal (ADU) as a function of the number of incident photons per pixel II.4 for green (525 nm) and blue (460 nm) LED illumination. Three characteristic response regimes can be identified in both curves. Although this analysis provides only an approximate characterization compared to the more complex calibration procedures used by camera manufacturers [46], it nevertheless offers a useful first-order evaluation of the sensor performance, sufficient for the purposes of this work.

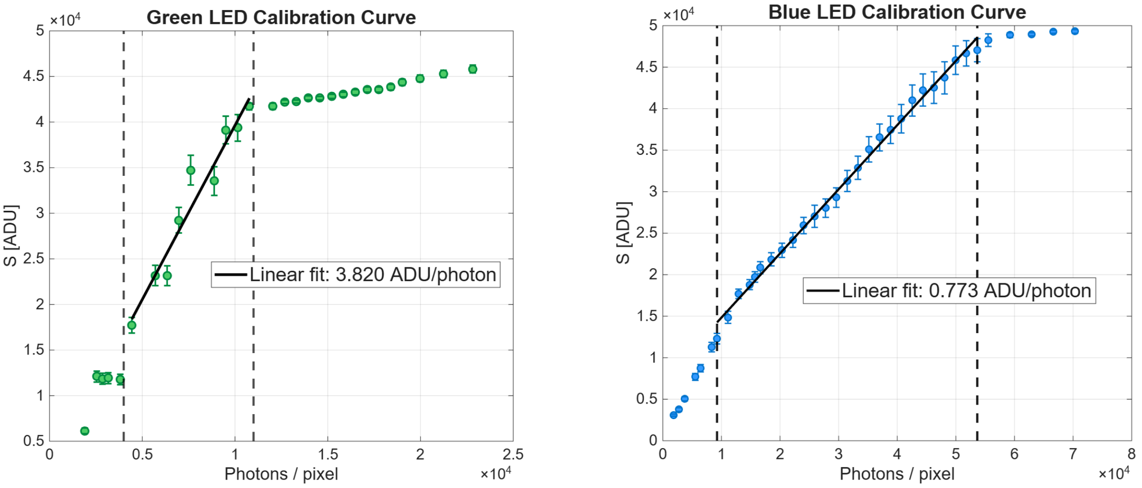

(a) (b)

Figure V.1: Calibration curves for (a) 525 nm green LED and (b) 480 nm blue LED, where a linear fit is applied at the regimes indicated by the vertical dashed lines.

Low-signal regime (Noise floor and sensitivity threshold)

At low photon counts, below the lower boundary of the linear regime indicated by the dashed lines, the measured signal is dominated by noise. For the green LED

(Fig. V.1a), this transition occurs at approximately 5×10^3 photons/pixel, whereas for the blue LED (Fig. V.1b) it occurs at approximately 9×10^3 photons/pixel. These values can therefore be regarded as the effective noise floor of the sensor for the respective wavelengths, representing the point at which the camera response deviates from linearity and the measured output becomes unreliable.

The behavior of the two calibration curves differs slightly in this regime. Under green illumination, the response exhibits a pronounced flattening, indicating that the recorded signal becomes nearly independent of the incident photon flux. In contrast, the blue illumination curve continues to decrease, but with strong and increasing deviation from linearity. Despite these differences, both regimes mark the practical lower detection limit of the camera sensor.

The transition values between the noise-dominated and linear regimes also provide an estimate of the minimum detectable photon count for low-light imaging applications. In this thesis, these sensitivity thresholds were used to theoretically estimate the minimum number of luciferase enzymes per pixel required to generate a detectable bioluminescent signal during a 150 ms exposure time (see Appendix C). The lower threshold observed for green illumination indicates slightly higher sensitivity at this wavelength, although additional measurements would be required to confirm this behavior quantitatively.

Lastly, according to published characterization data for a CMOS sensor comparable to the one used in this work, the expected noise floor is on the order of 3–10 photons/pixel [46]. The substantially higher values obtained in the present measurements are primarily attributed to background illumination from the green indicator LED, which was present during the calibration experiments, as well as to other limitations of the laboratory setup, including source instability, alignment inaccuracies, and measurement uncertainties. The effect of the indicator LED is particularly evident in the green-light calibration, where the response deviates from linearity and tends to flatten at low signal levels. Since the measurements were acquired as RGB images and subsequently separated into individual color channels, the green calibration retains a significant fraction of the background originating from the green indicator LED. In contrast, the blue-light calibration is less affected because only the blue channel was analyzed, thereby rejecting much of the green background contribution. This likely explains the more linear behavior observed in the blue calibration compared with the green calibration. Furthermore, adopting a less stringent linearity criterion for the green calibration would likely reduce the estimated detection threshold to approximately 10–50 photons, bringing the obtained values into closer agreement with those reported in the literature for comparable

CMOS sensors. Nevertheless, the measurements provide a transparent and realistic first-order characterization of the sensor's performance.

Linear regime (Responsivity)

In the intermediate region, in between the dashed lines, the sensor exhibits an approximately linear response. We determined the linear fitting ranges using a goodness-of-fit criterion. In this approach, the coefficient of determination R^2 quantifies the degree of linearity, while the relative Root Mean Square Error (RMSE) measures the deviation magnitude relative to the signal level. By defining acceptable threshold values for these parameters, we identified the ranges over which the calibration curve could be considered reliably linear [47].

For blue illumination, the linear fit yields a dynamic range extending from approximately 9250 to 53650 photons/pixel, with a coefficient of determination of $R^2 = 0.9953$ and a relative RMSE of 2.3%. In comparison, the green illumination fit produces a linear dynamic range from approximately 4000 to 10778 photons/pixel, with $R^2 = 0.9432$ and a relative RMSE of 6.1%. In both cases, the identified linear dynamic ranges span less than one order of magnitude in photon flux. Furthermore, the linearity criterion for the green illumination is comparatively more relaxed, indicating a less strictly linear sensor response in this regime.

The obtained slopes represent the effective conversion from incident photons to digital units (ADU) and are defined as the responsivity in Section II.1.2. We measured responsivities of $R_{\text{green}} = 3.820$ ADU/photon for green illumination and $R_{\text{blue}} = 0.773$ ADU/photon for blue illumination. This corresponds to an experimental responsivity ratio ($R_{\text{green}}/R_{\text{blue}}$) of approximately 4.95.

For comparison, the relative responsivity ratio estimated from the manufacturer spectral response data shown in Fig. II.3 is approximately 1.28, calculated as the ratio of the responsivities at 525 nm (0.87) and 460 nm (0.68) extracted from the spectral response plot. The discrepancy of a factor of 3.9 between the experimental and theoretical ratios is again likely a consequence of the non-ideal experimental conditions discussed previously. Additional uncertainty is introduced by the estimation of the manufacturer responsivity values, which were obtained by manually extracting data points from the published spectral response curve using visual inspection and ruler measurements.

High-signal regime (Saturation and Full Well Capacity)

At high photon counts, both curves exhibit a clear deviation from linearity and eventually saturate. The onset of saturation occurs at approximately $\sim 4.3 \times 10^4$ photons/pixel for green illumination and $\sim 4.8 \times 10^4$ photons/pixel for blue illumination. These values can be interpreted as estimates of the effective full well capacity in units of incident photons. The earlier saturation observed for green light is consistent with its higher responsivity, as the pixel reaches its maximum digital output at a lower photon count.

Overall Discussion

Overall, in the context of biosensing, a wide linear dynamic range, such as that observed for the blue illumination, is advantageous because it enables the detection of biomarker concentrations spanning multiple orders of magnitude without requiring additional adjustments, such as changes in exposure time. However, for ultra-low-light biosensing applications, the most critical parameter remains the sensitivity threshold, as it determines the minimum detectable signal and therefore limits performance in extremely low-concentration regimes potentially approaching single-molecule detection. For applications involving higher biomarker concentrations, which are beyond the scope of this thesis, the situation is partially reversed. In such cases, high responsivity, although beneficial for low-light detection, can also lead to earlier signal saturation, thereby reducing the ability to accurately measure high photon fluxes.

V.2 Expressed Proteins Characterization

This subsection presents the results of the characterization of proteins expressed in the laboratory, as described in Chapter III: Bioluminescence.

V.2.1 Concentration

The parameters used for protein concentration calculations described in Section III.3.2, along with the resulting concentrations of NanoLuc–SpyTag3 and BSA–SpyCatcher3 in micromolar units, are summarized in Table V.1. The NanoDrop instrument directly provides the absorbance and the optical path length. The molar extinction coefficient is obtained from the ExPASy database [48] by inputting the corresponding protein sequence, assuming the buffer is known.

Name	**Buffer**	**Absorbance (280 nm)**	ε **(M^{-1}cm^{-1})**	l **(cm)**	c **(μM)**
NanoLuc–SpyTag3	PBS	0.746	28420	1	≈ 26
BSA–SpyCatcher3	PBS	0.627	61375	1	≈ 10

Table V.1: Protein concentration measurements obtained using NanoDrop UV–Vis spectroscopy. Extinction coefficients were calculated using ExPASy based on the protein sequences.

NanoLuc–SpyTag3 shows higher expression than BSA–SpyCatcher3, although both appear to be within the same order of magnitude based on the absorbance measurements, as expected from the use of a common expression protocol. It is important to note, however, that these concentrations are derived from A280 measurements, which assume sample purity. Since the NanoDrop does not distinguish between different absorbing species, the reported concentration for BSA–SpyCatcher3 is likely overestimated due to the presence of impurities. Thus, the SDS–PAGE gel results described in the following subsection provide a more reliable indicator of expression success.

It is furthermore worth noting, that in the case of NanoLuc, expression can also be directly verified by the addition of its substrate and the resulting luminescence signal. In contrast, BSA–SpyCatcher3 lacks a direct functional readout, and its expression must therefore be assessed indirectly, for example by evaluating its binding capability in solution, as reflected in the SDS–PAGE results presented in the next subsection.

V.2.2 PROTEIN SIZE AND PURITY

The SDS-PAGE gel described in Section III.3.3, contains five channels, of which channels 1 (CH1), 3 (CH3), and 5 (CH5) are relevant for the purposes of this thesis. Channel 1 contains a mixture of equal concentrations of BSA–SpyCatcher3 and NanoLuc–SpyTag3, channel 3 contains NanoLuc–SpyTag3 alone and channel 5 contains BSA–SpyCatcher3 alone. As shown in Fig. V.2, a clear band appears in channels 1 and 3 at approximately 23 kDa, consistent with the expected molecular weight of NanoLuc–SpyTag3 (19 kDa for NanoLuc plus 4 kDa for linker + SpyTag3 + His6). The band is more intense in channel 3, which contains only NanoLuc–SpyTag3, while its lower intensity in channel 1 reflects the dilution. The absence of a band corresponding to the combined molecular weight of NanoLuc–SpyTag3 and BSA–SpyCatcher3 (100 kDa) indicates that formation of the conjugate is not observed under these conditions. However, given the lack of a clear band for BSA–SpyCatcher3 in channel 5, this result cannot be attributed

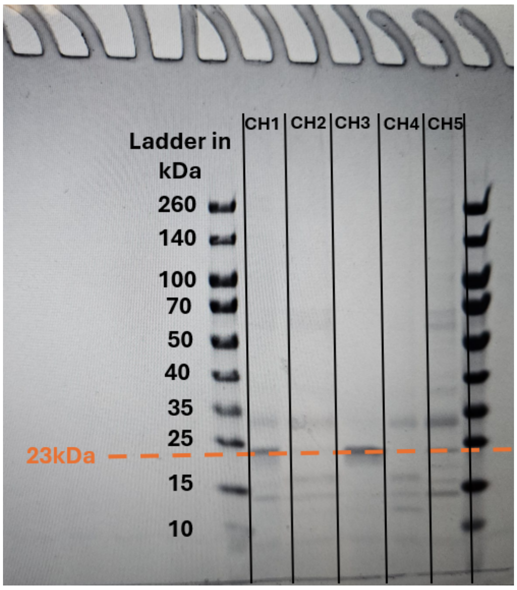

Figure V.2: SDS–PAGE gel showing the molecular weight ladder on one edge and five separate channels separated by black lines. The measured molecular mass of the successfully expressed NanoLuc luciferase is indicated in orange at approximately 23 kDa.

to inefficient binding alone, as the target protein may not have been successfully expressed or is present only at low purity.

A faint band at a similar molecular weight is also visible in channel 5, where NanoLuc is not expected, and is therefore likely due to background noise or nonspecific impurities rather than true NanoLuc contamination. Moreover, channel 5 lacks a distinct band at the expected size of BSA–SpyCatcher3 (79 kDa). Instead, multiple weak bands are observed, including faint signals around 60–70 kDa that may correspond to the target protein. Their low intensity suggests poor expression and/or partial degradation, consistent with the overall low purity of the sample.

Overall Discussion

Overall, only NanoLuc–SpyTag3 appears to be consistently and purely expressed. In contrast, BSA–SpyCatcher3 shows low expression and poor purity, and its concentration cannot be reliably determined from UV–Vis measurements due to significant sample contamination. Consequently, the binding interaction cannot be reliably assessed under these conditions, as insufficient expression and purity of BSA–SpyCatcher3 prevent a meaningful evaluation. It is also worth noting that binding behavior may differ between solution and surface-bound conditions, interactions observed in one environment may not directly translate to the other.

V.3 BASELINE BIOLUMINESCENCE MEASUREMENTS

In this section, we present the results of the baseline bioluminescence measurements, as described in Subsection IV.3. For all experiments, we acquired a negative control image of a sample containing NanoGlo substrate solution without luciferase. We used this measurement to account for both the intrinsic camera dark noise and any measurable auto-luminescence background signal originating from the substrate solution itself. During image processing and signal analysis, we subsequently used these images for background subtraction.

V.3.1 CMOS CAMERA CHIP DETECTION

In Figure V.3 we present representative bioluminescence measurements acquired at distinct NanoLuc concentrations with the CMOS-integrated platform. Using the previously established 460 nm calibration curve, we correlated the measured signal intensities with the corresponding estimated photon flux per pixel reaching the CMOS sensor.

1μM Concentration Point

The initial NanoLuc concentration of 1 µM, shown in Fig. V.3a, produced a strong baseline bioluminescent signal of 31481 ADU using a single 150 ms acquisition. This result is somewhat comparable with the theoretical estimations presented in Appendix C, where concentrations on the order of several hundred nanomolar were predicted to approach the CMOS sensor detection threshold.

100nM Concentration Point

Reducing the NanoLuc concentration to 100 nM and accumulating five sequential 150 ms images resulted in a comparable signal intensity of 37232 ADU, as shown in Fig. V.3b. Under ideal linear scaling conditions, approximately ten accumulated frames would have been required to reproduce the signal obtained at 1 µM. The observed deviation suggests that the 1 µM condition had already entered a substrate-limited regime, leading to partial depletion of the NanoGlo substrate and a reduced sustained photon emission during acquisition.

10nM Concentration Point

Further reduction of the NanoLuc concentration to 10 nM required accumulation of fifteen sequential 150 ms images to produce a measurable signal of 36484 ADU, as presented in Fig. V.3c. The resulting signal intensity approached that obtained for the 100 nM condition despite one order of magnitude lower enzyme concentration,

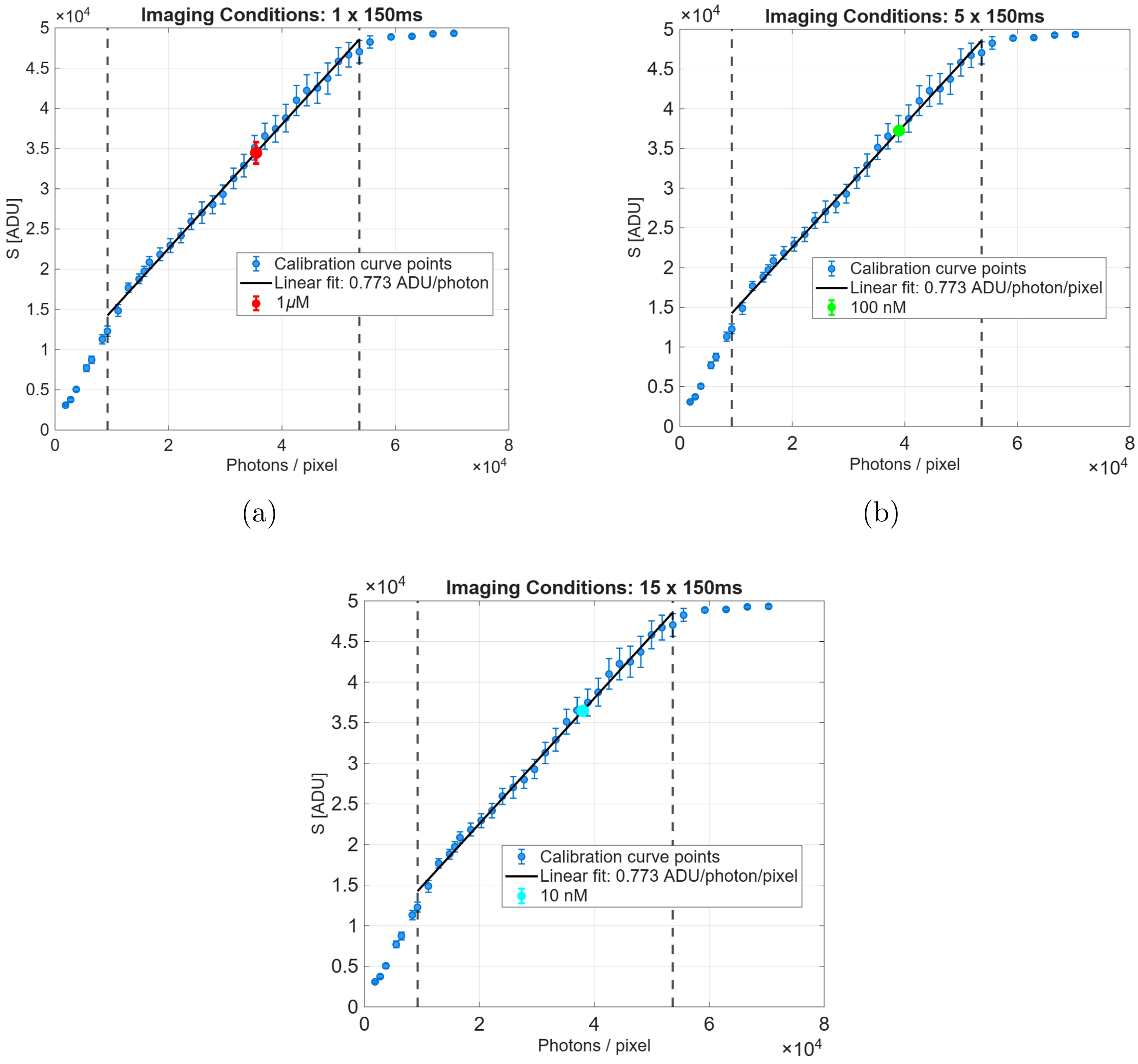

(a) (b) (c)

Figure V.3: Baseline bioluminescence measurements acquired using the CMOS camera-integrated platform. (a) Single 150 ms acquisition at 1 µM NanoLuc concentration (red point). (b) 100 nM NanoLuc measurement obtained through accumulation of 5 sequential 150 ms images (green point), showing comparable signal levels to the 1 µM condition in (a). (c) 10 nM NanoLuc measurement obtained through accumulation of 15 sequential 150 ms images (cyan point), illustrating continued signal detection at lower concentrations through temporal integration.

further indicating the onset of substrate-limited behavior at higher concentrations. In contrast to the 100 nM and 1 µM measurements, no significant signal decay was observed between consecutive acquisitions at 10 nM, suggesting that substrate depletion effects were substantially reduced in this concentration regime.

V.3.2 MICROSCOPE DETECTION

To provide a laboratory-reference measurement, we characterized the same NanoLuc dilution series using a conventional microscopy-based imaging system. Although no dedicated calibration curve was available for the microscopy setup, we assume the detector response to be approximately linear above the negative-control background level. The resulting measurements, shown in Fig. V.4, are plotted as signal intensity (ADU) versus NanoLuc molar concentration.

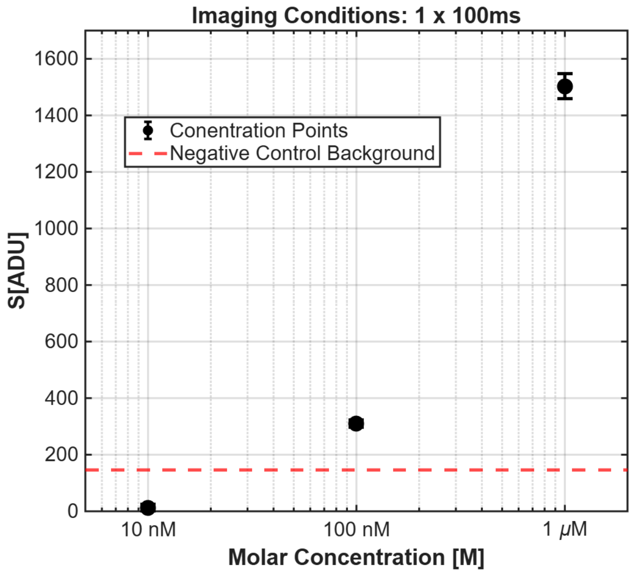

Figure V.4: Bioluminescent signal intensity measured using the microscopy-based detection setup as a function of NanoLuc concentration for a fixed exposure time of 100 ms. The red dashed line indicates the negative control background signal from the substrate.

In contrast to the CMOS-integrated platform, the microscope enabled direct detection of multiple NanoLuc concentrations using a single 100 ms acquisition without temporal frame accumulation, demonstrating a wider linear detection range and higher sensitivity under comparable conditions. In principle, the system should resolve approximately three orders of magnitude in concentration within the available 16-bit dynamic range above background level, however, the experiment reliably distinguished only two decades (1 µM and 100 nM). This limitation is likely caused by elevated background contributions from ambient light reaching the substrate from the underside of the microscope sample holder. Furthermore, the measured signals, namely 1503 ADU for 1 µM and 309 ADU for 100 nM, deviated from linear scaling, indicating substrate depletion effects similar to those seen in the CMOS-based measurements. Lastly, it is worth mentioning that despite operating with 16-bit image acquisition, the measured signal intensities remained relatively low even for longer exposure times tested but not presented here.

Overall Discussion

Overall, the presented results demonstrate that the CMOS-integrated platform was capable of detecting NanoLuc bioluminescence down to the 10 nM concentration range through temporal frame accumulation, while the microscopy-based setup reliably resolved concentrations down to 100 nM under the experimental conditions used here. Although the microscope provided higher sensitivity and a broader linear response range for single acquisitions, the CMOS platform achieved competitive low-concentration detection performance despite its significantly simpler and more compact architecture. This comparison would likely change in experiments where NanoLuc is immobilized on a surface, since the emitted signal would originate primarily from a confined two-dimensional region more closely matched to the focal plane of the microscope objective.

The theoretical estimation presented in Appendix C predicted that approximately 500 nM NanoLuc concentration would be required to reach the CMOS detection threshold of 15000 ADU for a single 150 ms acquisition. A fair comparison with the experimental measurements is obtained using the 10 nM condition, since this was the only concentration for which no measurable signal decay was observed during repeated acquisitions, consistent with the constant-emission assumption used in the theoretical model. The 10 nM measurement was obtained through accumulation of fifteen sequential 150 ms frames, corresponding to a total integration time of 2.25 s. Scaling the Appendix C model to the same effective integration time reduces the predicted threshold concentration from 500 nM to approximately 33.3 nM. Conversely, assuming approximate linear scaling in the experimentally observed low-concentration regime, the measured 10 nM signal of 36484 ADU corresponds to an estimated detection threshold concentration of approximately 4.1 nM at 15000 ADU. The remaining discrepancy of approximately one order of magnitude is considered reasonable given the simplifying assumptions of the theoretical model.

Several factors likely contribute to this deviation. First, the theoretical model assumes that each pixel receives photons only from a narrow column of solution directly above the sensor surface. In practice, photons emitted from a broader conical volume of the droplet can contribute to the measured signal through multiple propagation angles and scattering pathways, increasing the effective photon collection efficiency. Second, the calculations assume fully active and pure NanoLuc enzyme at the nominal concentration, whereas the effective active concentration following expression and sample preparation may differ. Finally, the assumed average photon emission rate of 8.6 photons per enzyme per second represents an approximate literature-based estimate and may vary under the experimental assay conditions used in this work.

Deviations from ideal linear concentration scaling were observed in both the CMOS and microscope measurements at higher NanoLuc concentrations. The primary interpretation is that substrate depletion contributed to the observed non-linear response, particularly for the 1 µM and 100 nM conditions where progressive signal decay was observed during repeated acquisitions. Independent support for this interpretation is provided by the signal decay plot in Appendix D, where a clear temporal signal decay was observed for NanoLuc concentrations of 1 µM. Nevertheless, additional factors may also contribute to the measured non-linearity, including sensor response non-linearity near the upper operating range, elevated background contributions, and accumulated read and dark noise during frame integration.

If anything, these findings highlight the potential of direct CMOS-based bioluminescence detection as a compact and cost-effective alternative for sensitive biochemical imaging applications.

V.4 Signal Enhancement

In this section, we present the results of the lock-in amplification experiments described in Subsection IV.3.1. We investigated two different modulation periodicities, namely 200,ms and 500,ms. For each case, we analyzed the recorded signal in both the time and frequency domains to evaluate the effectiveness of the lock-in amplification technique in isolating weak periodic signals from the background. We conducted both experiments over a total acquisition time of 90s with a frame rate of 100ms.

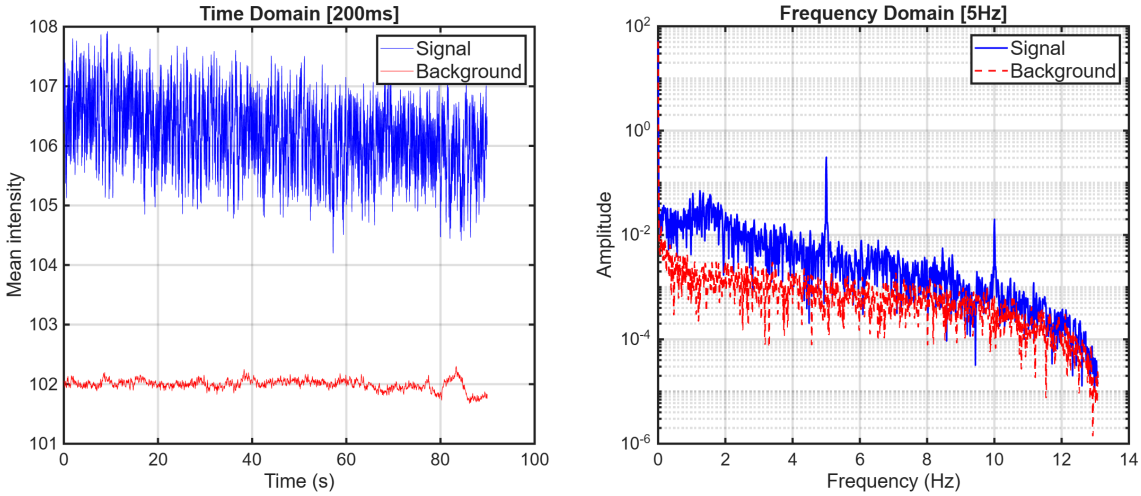

Figure V.5: Results acquired with the microscope for the 200 ms modulation periodicity: (a) signal in the time domain and (b) signal in the frequency domain.

Figure V.5(a) shows the temporal evolution of the signal for the 200 ms modulation periodicity. The measured intensity oscillates between an “on” state of approximately 107.5 and an “off” state of approximately 105.5, while the background level remains close to 102. Although a periodic modulation can be observed, the signal contrast relative to the background is relatively small and would normally be considered difficult to distinguish using direct observation alone.

An additional observation is that the signal does not fully return to the background level during the “off” state. This behavior can be quantified through the residual signal ratio:

$$R = \frac{I_{\text{off}} - I_{\text{bg}}}{I_{\text{on}} - I_{\text{bg}}} = 0.64 \tag{V.1}$$

where I_{on}, I_{off}, and I_{bg} correspond to the intensities of the on-state, off-state, and background, respectively. The 64% residual intensity suggests that the system does not have sufficient time to completely relax back to the background level before the next excitation cycle begins.

Figure V.5(b) presents the corresponding frequency-domain representation obtained through Fourier analysis. For a modulation periodicity of 200 ms, the expected reference frequency is:

$$f = \frac{1}{0.2\,\text{s}} = 5\,\text{Hz} \tag{V.2}$$

A clear spectral peak is observed at 5 Hz, confirming the presence of the modulated signal. In addition, a second weaker peak appears at 10 Hz, corresponding to the second harmonic of the fundamental frequency. The appearance of harmonics is expected because the modulation waveform is not perfectly sinusoidal. Rough transitions between the on and off states introduce higher-frequency components into the Fourier spectrum, leading to harmonic peaks at integer multiples of the fundamental frequency.

Figure V.6(a) shows the temporal response for the 500 ms modulation periodicity. In this case, the signal oscillates between an on-state intensity of approximately 107 and an off-state intensity close to 102.8, which is significantly closer to the background level. Compared to the 200 ms experiment, the longer modulation period allows the system additional time to relax during the off-state, resulting in improved signal separation between the active and inactive phases. This is confirmed and quantified with the residual ratio:

$$R = \frac{I_{\text{off}} - I_{\text{bg}}}{I_{\text{on}} - I_{\text{bg}}} = 0.16 \tag{V.3}$$

The corresponding frequency-domain spectrum is shown in Fig. V.6(b). For a modulation periodicity of 500 ms, the expected reference frequency is

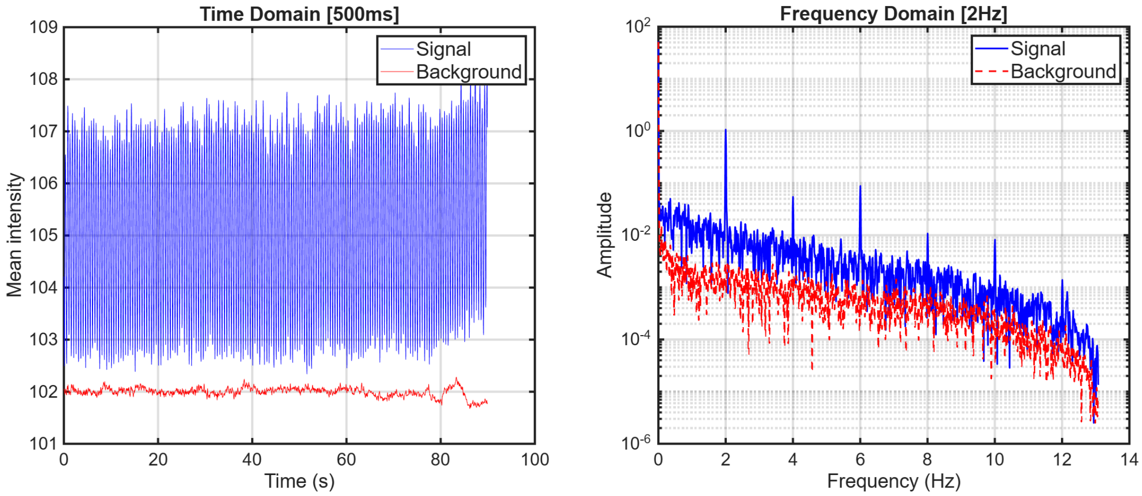

Figure V.6: Results acquired with the microscope for the 500 ms modulation periodicity: (a) signal in the time domain and (b) signal in the frequency domain.

$$f = \frac{1}{0.5\,\mathrm{s}} = 2\,\mathrm{Hz} \tag{V.4}$$

A dominant spectral peak is observed at 2 Hz, together with additional harmonic peaks at 4 Hz, 6 Hz, 8 Hz, 10 Hz, and 12 Hz.

Overall Discussion

Overall, the results demonstrate the effectiveness of lock-in amplification in detecting weak periodic signals embedded within an approximately random white-noise background, even when the modulation is not perfectly sinusoidal. In both experiments, distinct spectral peaks are observed at the expected reference frequencies together with higher-order harmonics originating from the abrupt switching behavior of the modulation signal. Furthermore, no significant differences in the overall effectiveness of the method are observed between the 200 ms and 500 ms modulation periodicities, highlighting the robustness of the signal enhancement technique.

VI Conclusions and Future Aspects

In this thesis, we demonstrated that a low-cost CMOS camera can be used as a biosensing detector for bioluminescent measurements despite its limited dynamic range and sensitivity (minimum 9000 photons/pixel). By combining longer exposure times with temporal signal interpolation and post-processing methods, weak bioluminescent signals could be successfully detected and quantitatively analyzed, when the sensor is properly characterized.

Unlike calibrated microscope systems, the CMOS detector used in this work required substantial characterization before reliable quantitative measurements could be performed. In the absence of dedicated optics, ambient light strongly influenced the measured signal. In addition both electronic read noise and several software-controlled parameters affected the digital output in non-transparent ways. As demonstrated throughout this thesis, achieving reliable bioluminescent measurements therefore depended not only on signal processing, but also on understanding the behavior and limitations of the sensor itself. In this sense, the complete characterization of a single CMOS detector could itself constitute an extensive independent research project.

Aside from the CMOS investigation, we also developed a bioluminescent probe. Exploring bioluminescence itself proved to be a particularly engaging journey, especially in the context of protein expression and characterization. While bioluminescence is traditionally used in biomedical imaging and reporter systems for living cells and organisms, this thesis demonstrates its potential in a more unconventional sensing application. The presented approach opens a pathway toward simpler and lower-cost bioluminescence-based detection platforms while preserving key advantages such as low background noise, high specificity (defined as the ability of a biosensor to selectively respond to the target analyte while minimizing responses to structurally similar or non-target species) and the absence of photobleaching. It is important to note, however, that establishing luciferase-catalyzed systems as reliable photon sources for optical biosensing requires further study and optimization, particularly regarding signal stability, as performance can depend on factors such as protein expression levels and the age of the system.

Finally, this work highlights that optics-free point-of-care optical biosensing devices can operate within two practical detection regimes. Above a device-dependent signal threshold (10 nM in the system presented here), reliable detection can be achieved through optimized acquisition strategies such as longer exposure times and temporal interpolation. Below this regime, intrinsic sensor limitations become increasingly significant, making signal enhancement strategies necessary for robust detection. In this context, this thesis also proposes an unconventional application of lock-in amplification, a technique commonly used in optoelectronics, for bioluminescent biosensing. Demonstrated here as a proof of concept in a microscope-based setup, this approach is particularly well suited to bioluminescence due to its low background noise and the absence of excitation light, advantages that are less accessible in fluorescence-based systems.

Future Aspects

As is often the case in scientific research, the deeper one investigates a subject, the more new questions and possibilities emerge. Throughout this thesis, several promising future research directions became apparent, many of which overlap like a Venn diagram within a broader biosensing and bioluminescence framework.

The first direction within diagnostic applications involves developing biomarker detection systems based on bioluminescent reporter assays, enabling true analyte-dependent biosensing rather than signals primarily scaling with luciferase concentration alone, as in this work. In particular, split-luciferase assay systems represent a promising platform for highly specific molecular sensing applications [49].

The second direction extends beyond simple detection toward the study of dynamic biological and biophysical processes requiring spatial information. Since bioluminescence avoids photobleaching, can theoretically remain bright for 1–2 hours [34], it is particularly attractive for long-term and real-time monitoring applications. One proposed approach was the localization of bioluminescent reporters on nanowires to provide spatially resolved information. Before such a system can be realized, an important open question remains: can nanowires enhance bioluminescent signals at all? This could not be conclusively answered here, as the intended binding system was unsuccessful. Initial experiments with bioluminescence in solution VI.1a showed no clear evidence of signal pickup or waveguiding by the nanowires in the line intesity profile taken half on nanowires and half on background solution VI.1b.

Furthermore, the CMOS sensor used in this work lacked the spatial resolution required to resolve individual nanowires, as can be seen in Appendix B. Nevertheless, one could envision a future architecture in which nanowires are grown directly on top of individual CMOS pixels, enabling near-field and directional light collection.

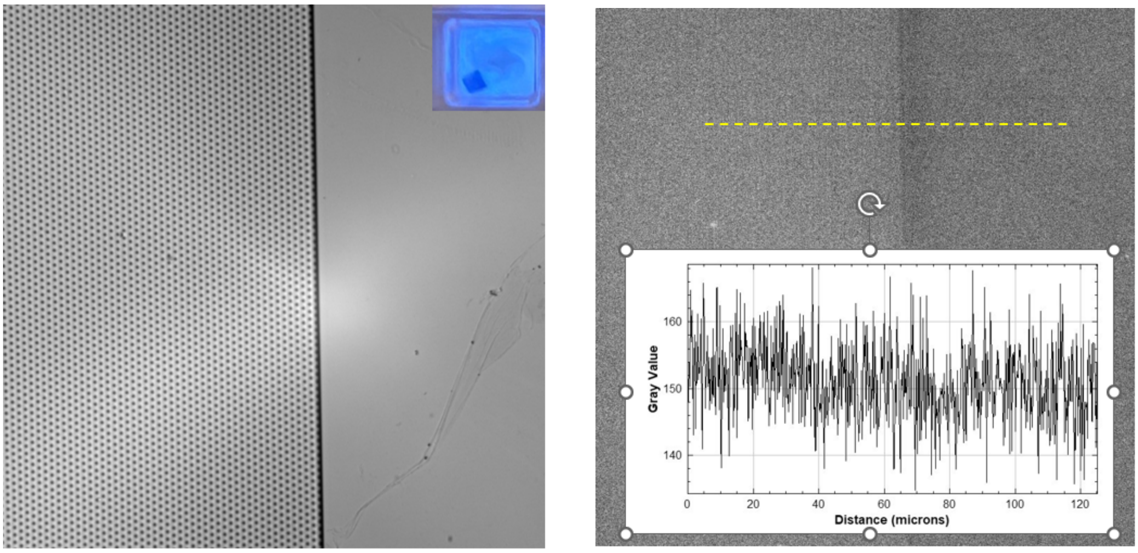

(a) (b)

Figure VI.1: (a)Nanowires immersed in a bioluminescent solution during in Bf microscope and phone acquired image (top right)(b) Measured line-profile intensity, with BF lamp off, comparing nanowire regions and the surrounding bioluminescent background solution.

The third direction focuses on on-chip signal enhancement strategies, particularly the implementation of lock-in amplification directly on the sensor. Rather than operating in the time domain, this approach could use spatial periodicity and frequency analysis in reciprocal space (k-space). Periodically spaced bioluminescent emitters could enable single-image acquisition, simplifying and accelerating detection. The proposed spatial scales are motivated by analogy with the temporal modulation experiments, where a modulation period of 200 ms was selected to match the typical image acquisition time of the camera, ensuring that the signal remained effectively constant during a single exposure. Similarly, in the spatial domain, the periodicity should be sufficiently large to be resolved by the imaging system while still allowing a large number of repeated cycles within the field of view to generate a distinct frequency-domain peak. As demonstrated for temporal modulation, the required periodicity could remain relatively large (mm scale), reducing fabrication complexity. However, generating a sufficiently strong frequency-domain peak would still require many periodic cycles (∼100), leading to practical space constraints. Possible solutions include exploiting periodic nanowire arrays (∼2.5 μm spacing) or deterministic lateral displacement (DLD) arrays with spacings of 20–100 μm, which are already available in our laboratory infrastructure.

Together, these future directions suggest that low-cost CMOS-based bioluminescence detection systems may evolve beyond proof-of-concept demonstrations into versatile platforms for biological sensing, quantitative analysis, and dynamic imaging applications.

A Dark Current Investigation

A supplementary investigation evaluated whether rapid CMOS sensor self-heating during operation could introduce significant temperature-dependent dark current during low-light measurements. To investigate this effect, the sensor temperature was monitored using an infrared (IR) camera while dark frames were simultaneously acquired. The average chip temperature was extracted from a region of interest centered on the sensor using an assumed emissivity of $\epsilon = 0.95$, as seen in Fig.A.1a.

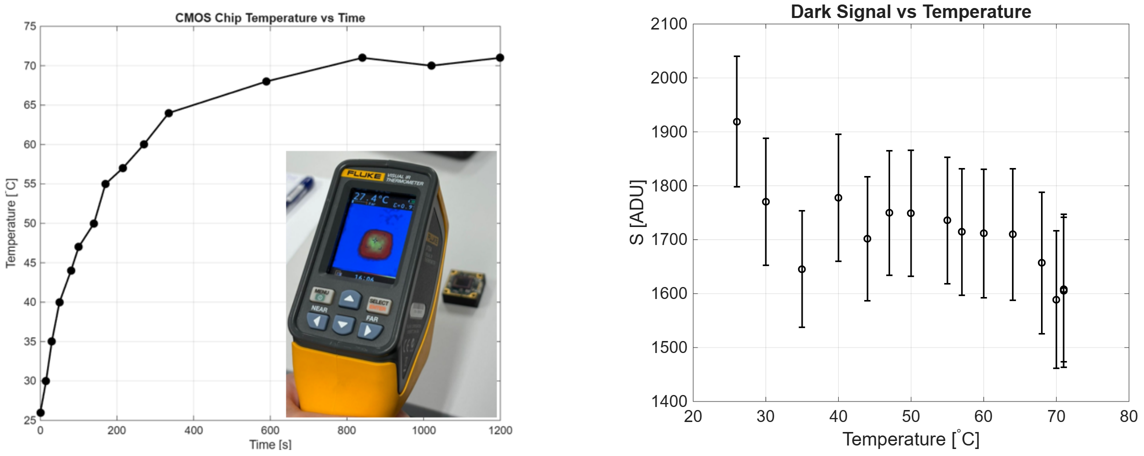

(a)

(b)

Figure A.1: (a) CMOS sensor temperature as a function of time after powering the device, with attached image of the IR camera used. (b) Measured dark signal as a function of sensor temperature.

As shown in Fig. A.1b, the sensor temperature increased from approximately 26°C to 70°C within about 10 minutes of operation. However, the measured dark signal remained approximately constant at ~ 1750 ADU over the investigated temperature range, as shown in Fig. A.1b. The absence of a clear temperature dependence suggests that the measured signal was dominated primarily by a fixed electronic offset and readout noise rather than thermally generated dark current. Nevertheless, a weak temperature-dependent contribution cannot be excluded due to the relatively large measurement scatter and the lack of full thermal equilibrium during acquisition, as recommended by the EMVA 1288 standard [14].

B SMALLEST DETECTABLE FEATURE INVESTIGATION

A supplementary experiment was performed to estimate the minimum detectable feature size of the bare CMOS imaging configuration. This investigation was motivated by the proposed use of nanowires as a signal-enhancement strategy, raising the question of whether individual nanowires with diameters of approximately 30 nm could be resolved by the CMOS sensor, and more generally, what the smallest detectable feature size of the system would be. To investigate this, bead suspensions containing particles of different diameters were deposited directly onto the CMOS sensor and imaged without additional optics. For comparison, the same samples were also imaged using a conventional microscope.

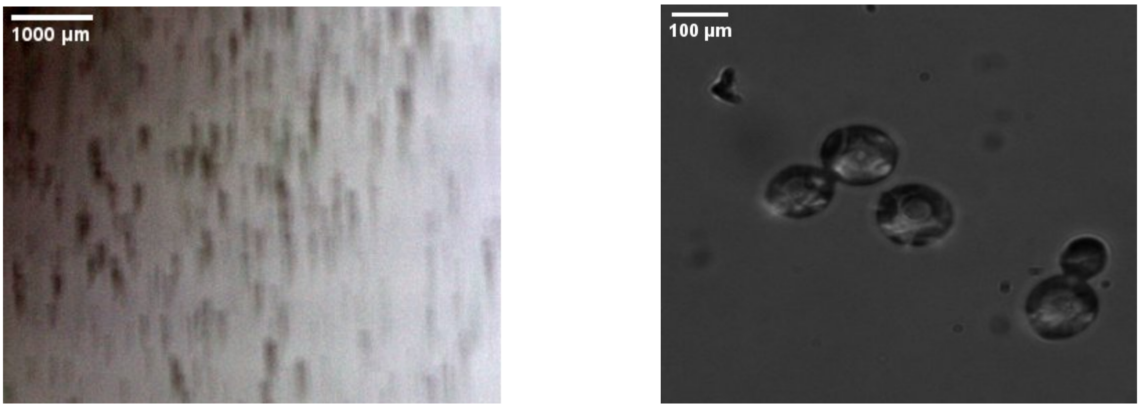

(a) (b)

Figure B.1: Images of nickel (Ni) beads with an average diameter of approximately 120 μm acquired using (a) the bare CMOS sensor and (b) a microscope with 20× magnification.

Among the tested samples, only the nickel beads with a diameter of approximately 120 μm produced a clearly detectable signal using the CMOS sensor. As shown in Fig. B.1a, the CMOS image appears blurred due to the absence of imaging optics, whereas the microscope image in Fig. B.1b resolves the bead structures with significantly higher sharpness and contrast. To quantify detectability, a line intensity profile was extracted across a representative nickel bead from the CMOS image, as shown in Fig. B.2. The profile exhibits a clear intensity decrease relative to the surrounding background, corresponding to an estimated contrast of approximately 56%.

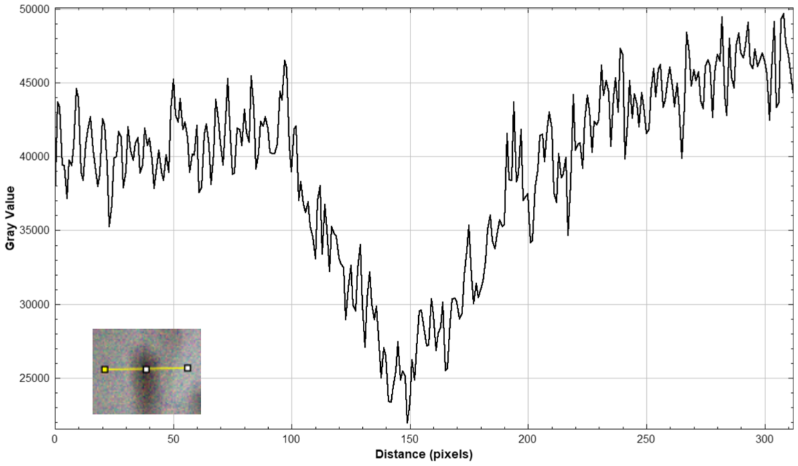

Figure B.2: Line intensity profile extracted across a representative nickel bead in the CMOS image shown in Fig. B.1a.

These results indicate that, under the investigated conditions, features on the order of 120 μm represented the smallest structures that could be robustly detected using the bare CMOS sensor configuration, while smaller beads did not produce distinguishable contrast above the background noise level.

C NanoLuc Detection Threshold

Here we estimate the minimum NanoLuc luciferase concentration required for detection based on the camera sensitivity threshold. The camera sensitivity at 460 nm is approximately $9 \cdot 10^3$ photons/pixel from results section V.1. Additionally, we know from the theory section Section III.2 that each NanoLuc enzyme produces approximately 10 photons/second. So for a standard 150 ms standard single exposure image, one would need:

$$N = \frac{\text{sensitivity threshold per pixel}}{\text{photons per second per enzyme} \cdot \text{time exposure}} = 6{\cdot}10^3 \text{NanoLuc enzymes/pixel}$$

Now to estimate the molar concentration to which this corresponds, we assume that each pixel integrates photons originating from a liquid volume directly above it Fig.C.1. The pixel size is approximately 2x2μm^2 and the effective liquid height is assumed to be 5mm, which corresponds to the typical imaging liquid volumes used in this work. So the end molar concetration is:

$$C = \frac{N}{\text{Avogadro's number} \cdot \text{collection volume}} = 500\,\text{nM}$$

This estimate suggests that a droplet containing NanoLuc at concentrations on the order of 500 nM in the presence of furimazine substrate should produce sufficient bioluminescence to be detected by the camera under the imaging conditions used in this thesis.

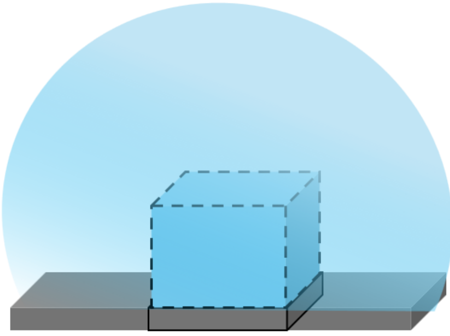

Figure C.1: Schematic illustration of a bioluminescent liquid droplet positioned above the CMOS pixel array. The dashed lines above one pixel indicate the effective detection volume from which emitted photons are collected into that pixel.

D Bioluminescent Signal Decay

Although the luciferase did not successfully bind inside the microfluidic channel during the signal enhancement experiments as originally intended, a measurable amount of protein remained trapped near the inlet region of the device. This can be clearly observed in Fig. D.1(c), where the substrate emission appears localized at the inlet while no significant signal is detected along the channel itself. Despite this limitation, the emitted bioluminescent signal was sufficiently strong to be imaged using the microscope system, as shown in Fig. D.1(a).
The recorded signal was further analyzed over a period of 90 s in order to evaluate its temporal stability. Figure D.1(b) presents the evolution of the mean signal intensity as a function of time together with the corresponding background level indicated by the red dashed line. A clear decay in the bioluminescent intensity is observed throughout the measurement duration, indicating the gradual depletion or deactivation of the luciferase–substrate reaction under the experimental conditions used in this work.

It should be noted that the decay dynamics are highly sensitive to several experimental parameters, including the luciferase-to-substrate concentration ratio, protein expression quality and purity, sample age, and environmental conditions. Nevertheless, this type of measurement provides a useful first-order characterization method for luciferase-based systems. In particular, monitoring the signal decay over time offers a quantitative approach for evaluating experimental conditions and establishing reproducible protocols for future measurements involving bioluminescent proteins.

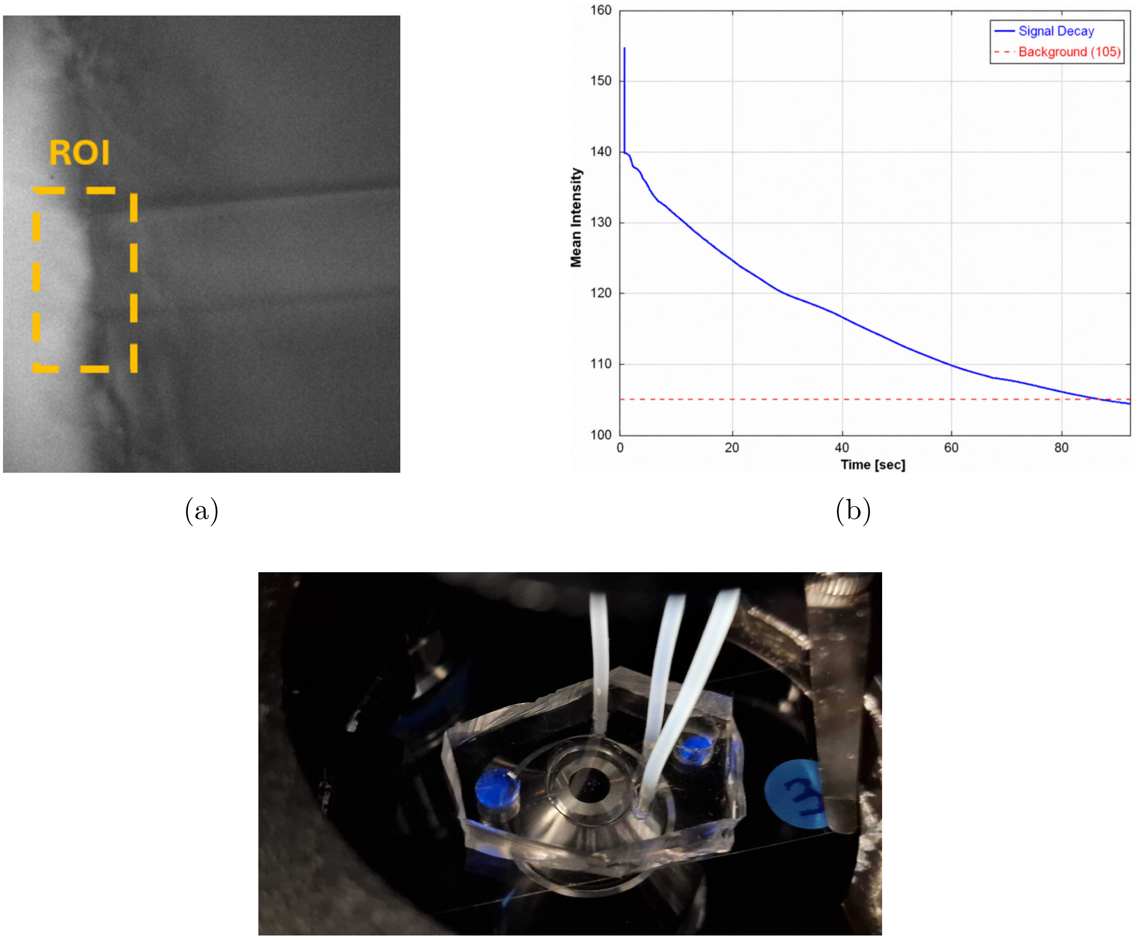

(a) (b) (c)

Figure D.1: (a) Microscope image of the measured signal ROI. (b) Mean signal intensity as a function of time over a 90 s acquisition period together with the background level (red dashed line). (c) Bioluminescent emission localized at the inlet region of the microfluidic device..

BIBLIOGRAPHY

[1] P. Mehrotra, "Biosensors and their applications – a review", Journal of Oral Biology and Craniofacial Research **6**, 153–159 (2016).

[2] P. Estrela, P. Damborský, J. Švitel, and J. Katrlík, "Optical biosensors", Essays in Biochemistry **60**, 91–100 (2016).

[3] B. Kaur et al., "Advancements in optical biosensing techniques: from fundamentals to future prospects", APL Photonics **9**, 091102 (2024).

[4] M. Cedrún-Morales, E. Soprano, G. Vanoni, A. Chandra, H. Iuele, F. Colella, S. Forciniti, V. Onesto, G. Grasso, G. Gigli, and L. L. del Mercato, "Advances in fluorescence-based point-of-care diagnostics: probes, nanostructures and integrated systems", Journal of Materials Chemistry C –, Review article on fluorescence-based POC devices, materials, and integrated platforms., – (2026).

[5] A. Altınışık Tağaç, P. Erdem, S. Seyhan Bozkurt, and M. Merdivan, "A customized microfluidic paper-based platform for colorimetric immunosensing: demonstrated via hcg assay for pregnancy test", Analytica Chimica Acta **1186**, Paper-based colorimetric pregnancy-test-style immunoassay for hCG detection., 339075 (2021).

[6] R. Davtyan, N. Anttu, J. Valderas-Gutiérrez, F. Höök, and H. Linke, "Image analysis optimization for nanowire-based optical detection of molecules", Nanophotonics, Published online September 30, 2024, `10.1515/nanoph-2024-0243` (2024).

[7] D. Verardo, F. W. Lindberg, N. Anttu, C. S. Niman, M. Lard, A. P. Dabkowska, T. Nylander, A. Månsson, C. N. Prinz, and H. Linke, "Nanowires for biosensing: lightguiding of fluorescence as a function of diameter and wavelength", Nano Letters **18**, 4796–4802 (2018).

[8] A. Drăgulinescu, "Applications of CMOS image sensors: state-of-the-art", Advanced Topics in Optoelectronics, Microelectronics, and Nanotechnologies **8411**, edited by P. Schiopu and R. Tamas, 84111D (2012).

[9] T. S. L. Gerald C. Holst, "1. introduction", in *Cmos/ccd sensors and camera systems*, 2nd ed. (SPIE Press, City, Country, 2011), pp. 7–9.

[10] J. Lai, "The principle and design of cmos active pixel sensor", Highlights in Science, Engineering and Technology **32**, 143–149 (2023).

[11] R. Gove, "7 - complementary metal-oxide-semiconductor (cmos) image sensors for mobile devices", in *High performance silicon imaging*, edited by D. Durini (Woodhead Publishing, 2014), pp. 191–234.

[12] Evident Scientific, *Cmos image sensors: how they work in digital microscopy*, Accessed: 2026-04-30, (n.d.) `https://evidentscientific.com/en/microscope-resource/knowledge-hub/digital-imaging/cmosimagesensors`.

[13] LUCID Vision Labs, *Understanding digital image sensors*, Accessed: 2026-04-30, (n.d.) `https://thinklucid.com/tech-briefs/understanding-digital-image-sensors/`.

[14] European Machine Vision Association (EMVA), *Emva standard 1288: standard for characterization of image sensors and cameras*, tech. rep. Release 3.1 (European Machine Vision Association, Germany, Dec. 2016).

[15] D. Hessman, *Optoelectronics lecture notes: 9. cameras*, Lund University, Lecture notes, <2025>.

[16] Basler AG, *Daa3840-45uc product documentation*, `https://docs.baslerweb.com/daa3840-45uc`, Accessed: 2026-04-29.

[17] T. S. L. Gerald C. Holst, "6.4 noise", in *Cmos/ccd sensors and camera systems*, 2nd ed. (SPIE Press, City, Country, 2011), pp. 174–178.

[18] T. S. L. Gerald C. Holst, "6.2 dark current", in *Cmos/ccd sensors and camera systems*, 2nd ed. (SPIE Press, City, Country, 2011), pp. 170–171.

[19] T. S. L. Gerald C. Holst, "6.4.6 pattern noise", in *Cmos/ccd sensors and camera systems*, 2nd ed. (SPIE Press, City, Country, 2011), pp. 181–182.

[20] J.-M. Woo, H.-H. Park, H. S. Min, Y. J. Park, S.-M. Hong, and C. H. Park, "Statistical analysis of random telegraph noise in cmos image sensors", in Sispad: 2008 international conference on simulation of semiconductor processes and devices, International Conference on Simulation of Semiconductor Processes and Devices, Hakone, JAPAN, SEP 09-11, 2008 (Japan Soc Appl Phys; IEEE Electron Devices Soc; Osaka Univ, Global COE Program, Ctr Elect Device Innovat; Keio Univ, Global COE Program, High Level Global Cooperat Leading Edge Platform Access Spaces; Inst Elect, Informat & Commun Engineers; IEEE EDS, Japan Chapter; IEEE EDS, Kansai Chapter, 2008), pp. 77+.

[21] E. Bolmanis, S. Uhlendorff, M. Pein-Hackelbusch, V. Galvanauskas, and O. Grigs, "Anomaly detection and removal strategies for in-line permittivity sensor signal used in bioprocesses", Frontiers in Bioengineering and Biotechnology **Volume 13 - 2025**, `10.3389/fbioe.2025.1609369` (2025).

[22] Basler AG, *Software downloads (pylon software suite)*, `https://www.baslerweb.com/en/downloads/software/?downloadCategory.values.label.data=pylon`, Accessed: 2026-04-29.

[23] *Gamma correction - an overview*, Accessed: 2026-04-30. Describes gamma as power-law transform: "Gamma correction is simply a power law transform...", 2023.

[24] M. Ramesh, R. Janani, C. Deepa, and L. Rajeshkumar, “Nanotechnology-enabled biosensors: a review of fundamentals, design principles, materials, and applications”, BIOSENSORS-BASEL **13**, `10.3390/bios13010040` (2023).

[25] S.-B. Kim and R. Paulmurugan, “Bioluminescent imaging systems for assay developments”, ANALYTICAL SCIENCES **37**, 233–247 (2021).

[26] Ylem and Ak ccm, *Panellus stipticus*, Public domain image from Wikimedia Commons, (2010) `https://commons.wikimedia.org/w/index.php?curid=17855618` (visited on 04/24/2026).

[27] Art Farmer, *Firefly w/ glow*, CC BY-SA 2.0, (2012) `https://commons.wikimedia.org/w/index.php?curid=7339552` (visited on 04/24/2026).

[28] A. Roda, M. Guardigli, E. Michelini, and M. Mirasoli, “Bioluminescence in analytical chemistry and in vivo imaging”, TrAC Trends in Analytical Chemistry **28**, 307–322 (2009).

[29] J. R. Lakowicz, *Principles of fluorescence spectroscopy*, 3rd ed. (Springer, New York, 2006).

[30] D. M. Close, S. Xu, G. S. Sayler, and S. B. Ripp, “In vivo bioluminescent imaging (bli): noninvasive visualization and interrogation of biological processes in living animals”, Sensors **10**, 180–206 (2010).

[31] A. H.-W. Yeh, C. Norn, Y. Kipnis, D. Tischer, S. J. Pellock, D. Evans, P. Ma, G. R. Lee, J. Z. Zhang, I. Anishchenko, B. Coventry, L. Cao, J. Dauparas, S. Halabiya, M. DeWitt, L. Carter, K. N. Houk, and D. Baker, “De novo design of luciferases using deep learning”, NATURE **614**, 774+ (2023).

[32] X. Zhou, S. Mehta, and J. Zhang, “Genetically encodable fluorescent and bioluminescent biosensors light up signaling networks”, Trends in Biochemical Sciences **45**, 889–905 (2020).

[33] A. Yevtodiyenko, A. Bazhin, P. Khodakivskyi, A. Godinat, G. Budin, T. Maric, G. Pietramaggiori, S. S. Scherer, M. Kunchulia, G. Eppeldauer, S. V. Polyakov, K. P. Francis, J. N. Bryan, and E. A. Goun, “Portable bioluminescent platform for in vivo monitoring of biological processes in non-transgenic animals”, Nature Communications **12**, 2680 (2021).

[34] M. P. Hall, J. Unch, B. F. Binkowski, M. P. Valley, B. L. Butler, M. G. Wood, P. Otto, K. Zimmerman, G. Vidugiris, T. Machleidt, M. B. Robers, H. A. Benink, C. T. Eggers, M. R. Slater, P. L. Meisenheimer, D. H. Klaubert, F. Fan, L. P. Encell, and K. V. Wood, “Engineered luciferase reporter from a deep sea shrimp utilizing a novel imidazopyrazinone substrate”, ACS CHEMICAL BIOLOGY **7**, 1848–1857 (2012).

[35]M. A. Klein, S. Lazarev, C. Gervasi, C. Cowan, T. Machleidt, and R. Friedman Ohana, “Luciferase calibrants enable absolute quantitation of bioluminescence power”, ACS Measurement Science Au **3**, 496–503 (2023).

[36]Promega Corporation, *Nano-glo® luciferase assay system technical manual*, Technical Manual TM369, Promega Corporation (Madison, WI, USA, 2022).

[37]Thermo Fisher Scientific, *A theoretical and practical guide for spectrophotometric determination of protein concentrations at 280 nm*, tech. rep., Technical Note, NanoDrop One/OneC and Multiskan Sky spectrophotometers (Thermo Fisher Scientific, 2018).

[38]B. Zakeri, J. O. Fierer, E. Celik, E. C. Chittock, U. Schwarz-Linek, V. T. Moy, and M. Howarth, “Peptide tag forming a rapid covalent bond to a protein, through engineering a bacterial adhesin”, Proceedings of the National Academy of Sciences **109**, E690–E697 (2012).

[39]A. H. Keeble, A. Banerjee, M. P. Ferla, S. C. Reddington, I. N. A. K. Anuar, and M. Howarth, “Evolving accelerated amidation by spytag/spycatcher to analyze membrane dynamics”, Proceedings of the National Academy of Sciences **116**, 26523–26533 (2019).

[40]J. Friend and L. Yeo, “Fabrication of microfluidic devices using polydimethylsiloxane”, Biomicrofluidics **4**, `10.1063/1.3259624` (2010).

[41]Y. Kim, J. Gonzales, and Y. Zheng, “Sensitivity-enhancing strategies in optical biosensing”, Small **17**, Epub 2020 Dec 28, e2004988 (2021).

[42]J. R. Mejía-Salazar and O. N. Oliveira Jr., “Plasmonic biosensing”, Chemical Reviews **118**, 10617–10625 (2018).

[43]S. J. Ward, R. Layouni, S. Arshavsky-Graham, E. Segal, and S. M. Weiss, “Signal processing techniques to reduce the limit of detection for thin film biosensors”, ACS Sensors **6**, Also available as arXiv:2103.07524, 2967–2978 (2021).

[44]Q. Zhang, W. Jeong, and D. J. Kang, “Lock-in amplifiers as a platform for weak signal measurements: development and applications”, Current Applied Physics **66**, 95–109 (2024).

[45]C. S. Niman, J. P. Beech, J. O. Tegenfeldt, P. M. G. Curmi, D. N. Woolfson, N. R. Forde, and H. Linke, “Controlled microfluidic switching in arbitrary time-sequences with low drag”, Lab on a Chip **13**, 2389–2396 (2013).

[46]Basler AG, *Emva 1288 standard compliant test report: daa3840-45um*, EMVA 1288 Datasheet, EMVA 1288 Standard Release 3.1 compliant (Basler AG, n.d.).

[47]N. R. Draper and H. Smith, *Applied regression analysis*, 3rd (John Wiley & Sons, New York, 1998) Chap. 1 and 11, pp. 35–45, 243–250.

[48] ExPASy, *Protparam tool*, `https://web.expasy.org/protparam/`, Accessed: 2025-05-13, 2025.

[49] T. Azad, A. Tashakor, and S. Hosseinkhani, “Split-luciferase complementary assay: applications, recent developments, and future perspectives”, Analytical and Bioanalytical Chemistry **406**, 5541–5560 (2014).